8. Kitada K, Ishishita S, Tosaka K, Takahashi R, Ueda M, et al. (2007) Transposon-tagged mutagenesis in the rat. Nat Methods 4: 131–133.
9. Zan Y, Haag JD, Chen KS, Shepel LA, Wigington D, et al. (2003) Production of knockout rats using ENU mutagenesis and a yeast-based screening assay. Nat Biotechnol 21: 645–651.
10. Smits BM, Mudde JB, van de Belt J, Verheul M, Olivier J, et al. (2006) Generation of gene knockouts and mutant models in the laboratory rat by ENU-driven target-selected mutagenesis. Pharmacogenet Genomics 16: 159–169.
11. Mashimo T, Yanagihara K, Tokuda S, Voigt B, Takizawa A, et al. (2008) An ENU-induced mutant archive for gene targeting in rats. Nat Genet 40: 514–515.
12. Yoshimi K, Tanaka T, Takizawa A, Kato M, Hirabayashi M, et al. (2009) Enhanced colitis-associated colon carcinogenesis in a novel Apc mutant rat. Cancer Sci.
13. Porteus MH, Carroll D (2005) Gene targeting using zinc finger nucleases. Nat Biotechnol 23: 967–973.
14. Wu J, Kandavelou K, Chandrasegaran S (2007) Custom-designed zinc finger nucleases: what is next? Cell Mol Life Sci 64: 2933–2944.
15. Hockemeyer D, Soldner F, Beard C, Gao Q, Mitalipova M, et al. (2009) Efficient targeting of expressed and silent genes in human ESCs and iPSCs using zinc-finger nucleases. Nat Biotechnol 27: 851–857.
16. Geurts AM, Cost GJ, Freyvert Y, Zeitler B, Miller JC, et al. (2009) Knockout rats via embryo microinjection of zinc-finger nucleases. Science 325: 433.
17. Noguchi M, Yi H, Rosenblatt HM, Filipovich AH, Adelstein S, et al. (1993) Interleukin-2 receptor gamma chain mutation results in X-linked severe combined immunodeficiency in humans. Cell 73: 147–157.
18. Leonard WJ (2001) Cytokines and immunodeficiency diseases. Nat Rev Immunol 1: 200–208.
19. Blunt T, Finnie NJ, Taccioli GE, Smith GC, Demengeot J, et al. (1995) Defective DNA-dependent protein kinase activity is linked to V(D)J recombination and DNA repair defects associated with the murine scid mutation. Cell 80: 813–823.
20. Kirchgessner CU, Patil CK, Evans JW, Cuomo CA, Fried LM, et al. (1995) DNA-dependent kinase (p350) as a candidate gene for the murine SCID defect. Science 267: 1178–1183.
21. Cao X, Shores EW, Hu-Li J, Anver MR, Kelsall BL, et al. (1995) Defective lymphoid development in mice lacking expression of the common cytokine receptor gamma chain. Immunity 2: 223–238.
22. DiSanto JP, Muller W, Guy-Grand D, Fischer A, Rajewsky K (1995) Lymphoid development in mice with a targeted deletion of the interleukin 2 receptor gamma chain. Proc Natl Acad Sci U S A 92: 377–381.
23. Ohbo K, Suda T, Hashiyama M, Mantani A, Ikebe M, et al. (1996) Modulation of hematopoiesis in mice with a truncated mutant of the interleukin-2 receptor gamma chain. Blood 87: 956–967.
24. Urnov FD, Miller JC, Lee YL, Beausejour CM, Rock JM, et al. (2005) Highly efficient endogenous human gene correction using designed zinc-finger nucleases. Nature 435: 646–651.
25. Kandavelou K, Ramalingam S, London V, Mani M, Wu J, et al. (2009) Targeted manipulation of mammalian genomes using designed zinc finger nucleases. Biochem Biophys Res Commun 388: 56–61.
26. Dao MA, Tsark E, Nolta JA (1999) Animal xenograft models for evaluation of gene transfer into human hematopoietic stem cells. Curr Opin Mol Ther 1: 553–557.
27. Thomsen M, Yacoub-Youssef H, Marcheix B (2005) Reconstitution of a human immune system in immunodeficient mice: models of human alloreaction in vivo. Tissue Antigens 66: 73–82.
28. Shultz LD, Ishikawa F, Greiner DL (2007) Humanized mice in translational biomedical research. Nat Rev Immunol 7: 118–130.
29. Ito M, Kobayashi K, Nakahata T (2008) NOD/Shi-scid IL2rgamma(null) (NOG) mice more appropriate for humanized mouse models. Curr Top Microbiol Immunol 324: 53–76.
30. Quintana E, Shackleton M, Sabel MS, Fullen DR, Johnson TM, et al. (2008) Efficient tumour formation by single human melanoma cells. Nature 456: 593–598.
31. Machida K, Suemizu H, Kawai K, Ishikawa T, Sawada R, et al. (2009) Higher susceptibility of NOG mice to xenotransplanted tumors. J Toxicol Sci 34: 123–127.
32. Doyon Y, McCammon JM, Miller JC, Faraji F, Ngo C, et al. (2008) Heritable targeted gene disruption in zebrafish using designed zinc-finger nucleases. Nat Biotechnol 26: 702–708.
33. Santiago Y, Chan E, Liu PQ, Orlando S, Zhang L, et al. (2008) Targeted gene knockout in mammalian cells by using engineered zinc-finger nucleases. Proc Natl Acad Sci U S A 105: 5809–5814.
34. Miller JC, Holmes MC, Wang J, Guschin DY, Lee YL, et al. (2007) An improved zinc-finger nuclease architecture for highly specific genome editing. Nat Biotechnol 25: 778–785.

Diabetologia (2010) 53:1727–1731
DOI 10.1007/s00125-010-1744-6

SHORT COMMUNICATION

Angiotensin II type 1 receptor-independent beneficial effects of telmisartan on dietary-induced obesity, insulin resistance and fatty liver in mice

X. Rong · Y. Li · K. Ebihara · M. Zhao · J. Naowaboot · T. Kusakabe · K. Kuwahara · M. Murray · K. Nakao

Received: 4 January 2010 / Accepted: 4 March 2010 / Published online: 15 April 2010
© Springer-Verlag 2010

Abstract
Aims/hypothesis Evidence suggests that telmisartan, an angiotensin II type 1 receptor (AT1) blocker and peroxisome proliferator-activated receptor-γ partial agonist, has beneficial actions that limit development of the metabolic syndrome and diabetes. However, the role played by AT1 inhibition in metabolic effects elicited by telmisartan remains uncertain. Here we isolated the metabolic effects of telmisartan from AT1 antagonism.
Methods Male *At1a* (also known as *Agtr1a*)-deficient mice were fed a standard diet or 60% high-fat diet; those on high-fat diet were co-administered telmisartan (3 mg kg^{-1} day^{-1} by oral gavage) or vehicle for 12 weeks.
Results In *At1a*-null mice, telmisartan prevented high-fat-diet-induced increases in (1) body weight, epididymal and inguinal white adipose tissue weight, adipocyte size and plasma leptin concentration; (2) plasma glucose and insulin concentrations and HOMA index; and (3) liver weight and triacylglycerol content. Insulin tolerance testing also indicated that telmisartan improved the high-fat-diet-induced reduction of glucose-lowering by insulin.
Conclusions/interpretation The present findings demonstrate beneficial, AT1-independent effects of the AT1 blocker telmisartan on dietary-induced obesity, insulin resistance and fatty liver in animals.

Keywords Angiotensin II type 1 receptor · Fatty liver · Insulin resistance · Obesity · Telmisartan

Abbreviations

ARB	Angiotensin II type 1 receptor blocker
AT1	Angiotensin II type 1 receptor
eWAT	Epididymal white adipose tissue
HFD	High-fat diet
ITT	Insulin tolerance test
iWAT	Inguinal white adipose tissue
KO	Knockout
PPAR	Peroxisome proliferator-activated receptor

Introduction

The metabolic syndrome is a cluster of conditions arising from overnutrition and a sedentary lifestyle. Common components of the metabolic syndrome include abdominal obesity, insulin resistance, hypertension and dyslipidaemia. Additional comorbidities may also be present, such as hepatic steatosis leading to non-alcoholic fatty liver disease, proinflammatory and prothrombotic states, and reproductive disorders [1]. Insulin resistance is the key component of the metabolic syndrome. It precedes and predicts the incidence and development of type 2 diabetes and cardiovascular diseases [2].

It has been suggested that activation of the renin–angiotensin system is a common feature in patients with

Electronic supplementary material The online version of this article (doi:10.1007/s00125-010-1744-6) contains supplementary material, which is available to authorised users.

X. Rong · Y. Li (✉) · K. Ebihara · M. Zhao · J. Naowaboot · T. Kusakabe · K. Kuwahara · K. Nakao
Department of Medicine and Clinical Science,
Kyoto University Graduate School of Medicine,
Kyoto 606-8507, Japan
e-mail: yuhao@kuhp.kyoto-u.ac.jp

M. Murray
Laboratory of Pharmacogenomics, Faculty of Pharmacy,
The University of Sydney,
Sydney, NSW 2006, Australia

obesity/the metabolic syndrome [2]. Indeed, blockade of the renin–angiotensin system has been shown in clinical and experimental studies to improve the metabolic syndrome [2]. Most of the established physiological and pathophysiological effects of angiotensin II appear to be mediated through the angiotensin II type 1 receptor (AT1). Angiotensin II type 1 receptor blockers (ARBs) have been used widely in the clinic as antihypertensive agents. More recently, treatment with some ARBs has been found to improve insulin resistance and to protect against the onset and development of type 2 diabetes in insulin-resistant patients with hypertension [2]. Studies in experimental animals seem to support clinical findings [2]. Thus, although the precise mechanisms have yet to be established, the contribution of AT1 signalling and the beneficial effects of AT1 inhibition in the metabolic syndrome are undoubted.

Telmisartan is a well-established ARB. Recently, it was shown to be a partial agonist of the peroxisome proliferator-activated receptor (PPAR)γ in cultured cells [3, 4] and to activate PPARα in cultured hepatic cells and in liver of wild-type mice fed a high-fat diet (HFD) [5]. Telmisartan has also been reported to improve HFD-induced obesity, insulin resistance and fatty liver in wild-type animals [4, 5]. However, the extent to which AT1 inhibition contributes to the beneficial effects of telmisartan treatment has not yet been established. The present study tests the role of AT1 inhibition in telmisartan-elicited metabolic effects using HFD-fed *At1a* (also known as *Agtr1a*)-knockout (KO) mice.

Methods

Animals, diet and experimental protocol All animal procedures were in accordance with the Principles of Laboratory Animal Care (http://grants1.nih.gov/grants/olaw/references/phspol.htm) and were approved by the Animal Ethics Committee, Kyoto University, Japan. Mice were housed in a temperature-controlled facility (21±1°C, 55±5% relative humidity) with a 12-h light/dark cycle (three to four mice per cage).

Male C57BL/6J wild-type mice were purchased from Japan SLC (Shizuoka, Japan). Male *At1a*-KO mice on a C57BL/6J background were generated by methods that have been described previously [6]. Animals (8 weeks of age) were divided into three groups (n=8–10 each): (1) standard diet control (standard diet Tel−); (2) HFD control (HFD Tel−); and (3) HFD telmisartan (HFD Tel+) groups. The animals had free access to water and the standard diet (CLEA, Tokyo, Japan) (Tel− group) or HFD (containing 20% [wt/wt] protein, 20% [wt/wt] carbohydrate and 60% [wt/wt] fat) (D12492; Research Diet, New Brunswick, NJ, USA) (HFD Tel− and HFD Tel+ groups). Animals receiving the HFD were also administered telmisartan (3 mg/kg suspended in 5% (wt/vol.) gum arabic (a gift from Boehringer Ingelheim, Tokyo, Japan) or vehicle by oral gavage once daily (between 11:00 and 12:00 hours) for 12 weeks. Daily (24 h) food intake was estimated from weekly measurements. Systolic BP was measured by a tail-cuff method (MK-2000ST; Muromachi Kikai, Tokyo, Japan) at week 5. Blood samples were collected by retroorbital venous puncture under ether anaesthesia at week10 in animals in non-fasted and fasted (12 h) states. Insulin tolerance tests (ITT; 0.75 IU/kg, i.p.; Humulin R-Insulin; Eli Lilly, Indianapolis, IN, USA) were conducted after fasting (6 h) at week11. After animals were weighed at week12, blood samples were collected again from non-fasted animals. Immediately thereafter animals were killed by prompt dislocation of the neck vertebra. Epididymal white adipose tissue (eWAT), inguinal white adipose tissue (iWAT) and liver were collected and weighed. Gastrocnemius was also collected. Glucose, triacylglycerol and NEFA concentrations were determined colorimetrically (Wako, Osaka, Japan), and insulin and leptin concentrations were analysed by ELISA (Morinaga, Tokyo, Japan). HOMA was calculated by method that has been described previously [7].

A portion of eWAT or liver was fixed with 10% formalin (vol./vol.) and embedded in paraffin. Sections (20 μm) were cut and stained with haematoxylin and eosin for examination of adipose tissue and liver histology (IX-81; Olympus, Tokyo, Japan). The adipocyte cross-sectional area was measured using an image analysing system (KS 400; Carl Zeiss Vision, Eching, Germany).

Data analysis All results are expressed as means ± SEM. Data were analysed by one-way ANOVA. If a difference was detected (F ratio), the Student–Newman–Keuls test was performed to locate the differences between groups. Values of $p<0.05$ were considered to be statistically significant.

Results

Consistent with previous reports [4, 5], we have demonstrated that telmisartan treatment (3 mg/kg) did not affect food intake (Electronic supplementary material [ESM] Fig. 1b), but substantially attenuated HFD-induced obesity (ESM Fig. 1c–h), insulin resistance (ESM Fig. 2a–e) and lipid overaccumulation in liver and skeletal muscle (ESM Fig. 3c–g) in C57BL/6J wild-type mice. In the present study, systolic BP in *At1a*-KO mice was 75±2.5 mmHg (Fig. 1a), which was lower than in wild-type mice (ESM Fig. 1a); telmisartan did not alter systolic BP in *At1a*-KO mice.

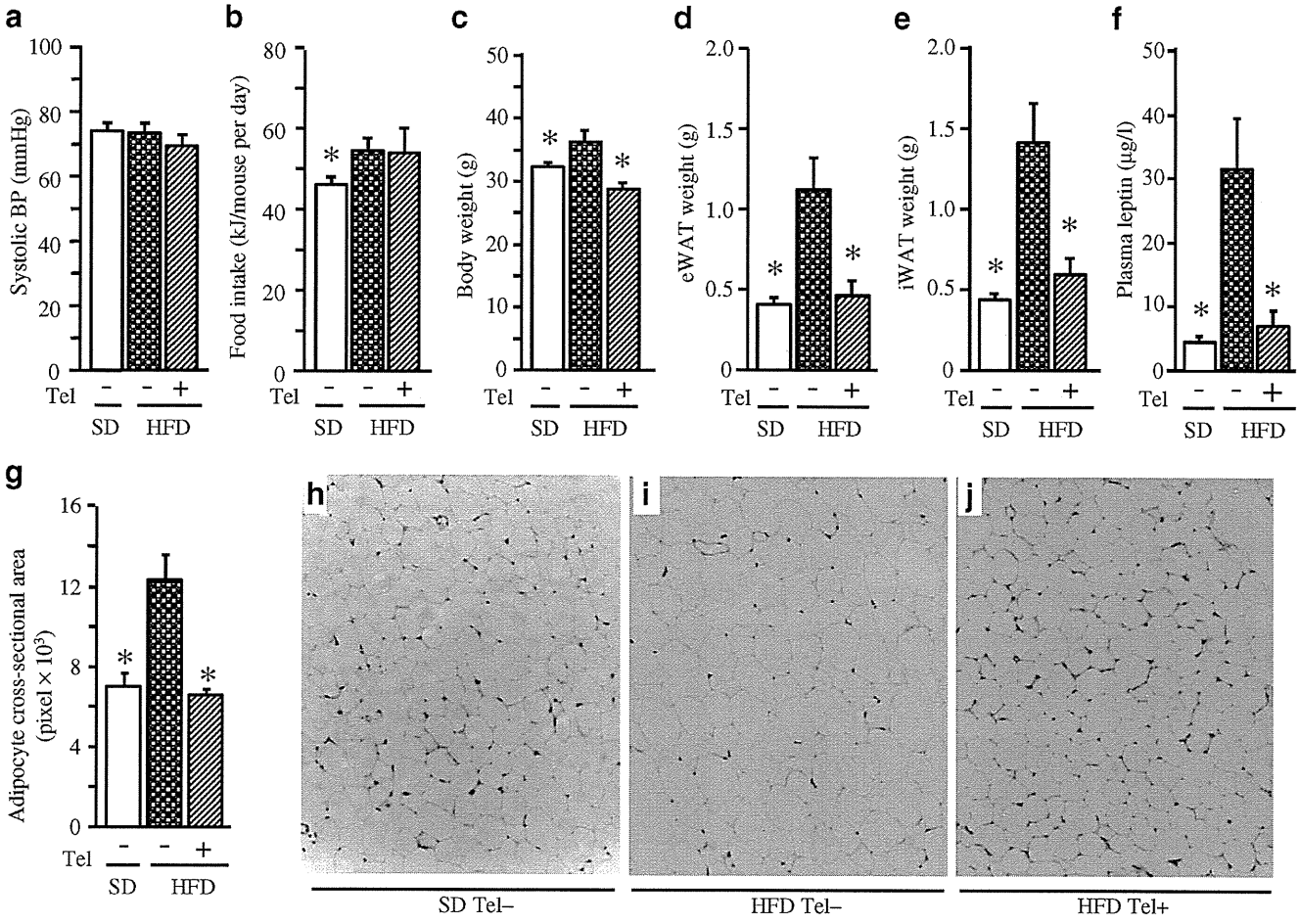

Fig. 1 Systolic BP (**a**), food intake per day (**b**), body weight (**c**), eWAT weight (**d**), iWAT weight (**e**), plasma leptin concentration (**f**), adipocyte cross-sectional area (**g**) and representative images (**h–j**) showing histology of eWAT (haematoxylin and eosin staining, magnification ×200) in male *Atl1*-KO mice fed standard or HFD for 12 weeks. All values are means ± SEM (n=8–10); *p<0.05 vs HFD control (Tel–). Tel–, vehicle; Tel+, telmisartan 3 mg/kg

HFD feeding significantly increased food intake (Fig. 1b), body weight (Fig. 1c), the weight of eWAT (Fig. 1d) and iWAT (Fig. 1e), adipocyte size (Fig. 1g–i) and plasma leptin concentration (Fig. 1f) in *Atl1*-KO mice. Telmisartan treatment did not affect food intake, but did ameliorate other variables (Fig. 1c–g, j).

In *Atl1*-KO mice, HFD feeding increased the fasted plasma glucose (Fig. 2a) and insulin (Fig. 2b) concentrations, and the HOMA index (Fig. 2c) in comparison with those in standard diet-fed *Atl1*-KO mice. Plasma glucose concentrations after insulin challenge (Fig. 2d) and the glucose AUC during ITT (Fig. 2e) were also increased by HFD treatment. Telmisartan treatment suppressed the HFD-induced increase in all variables.

HFD feeding had no effect on non-fasted and fasted plasma concentrations of triacylglycerol and NEFA (Fig. 2f, g), and on liver weight (Fig. 2h), whereas triacylglycerol content in liver and skeletal muscle was increased against that in standard diet-fed *Atl1*-KO mice (Fig. 2i, j). Telmisartan treatment decreased liver weight and triacylglycerol content in liver and skeletal muscle. Histological evaluation confirmed that fatty infiltration of the liver was decreased by telmisartan (data not shown). In contrast with the lipid-lowering effects observed in HFD-fed wild-type rats [4] and mice (ESM Fig. 3a, b), telmisartan minimally affected non-fasted and fasted plasma triacylglycerol and NEFA concentrations in HFD-fed *Atl1*-KO mice.

Discussion

The present study demonstrates that long-term treatment with telmisartan in *Atl1*-null mice fed a HFD prevents or improves the increase in: (1) body weight, white adipose tissue weight, adipocyte size and plasma leptin concentration; (2) plasma glucose and insulin concentrations, HOMA index, and plasma glucose concentrations and glucose AUC during ITT; and (3) liver weight and triacylglycerol content of the

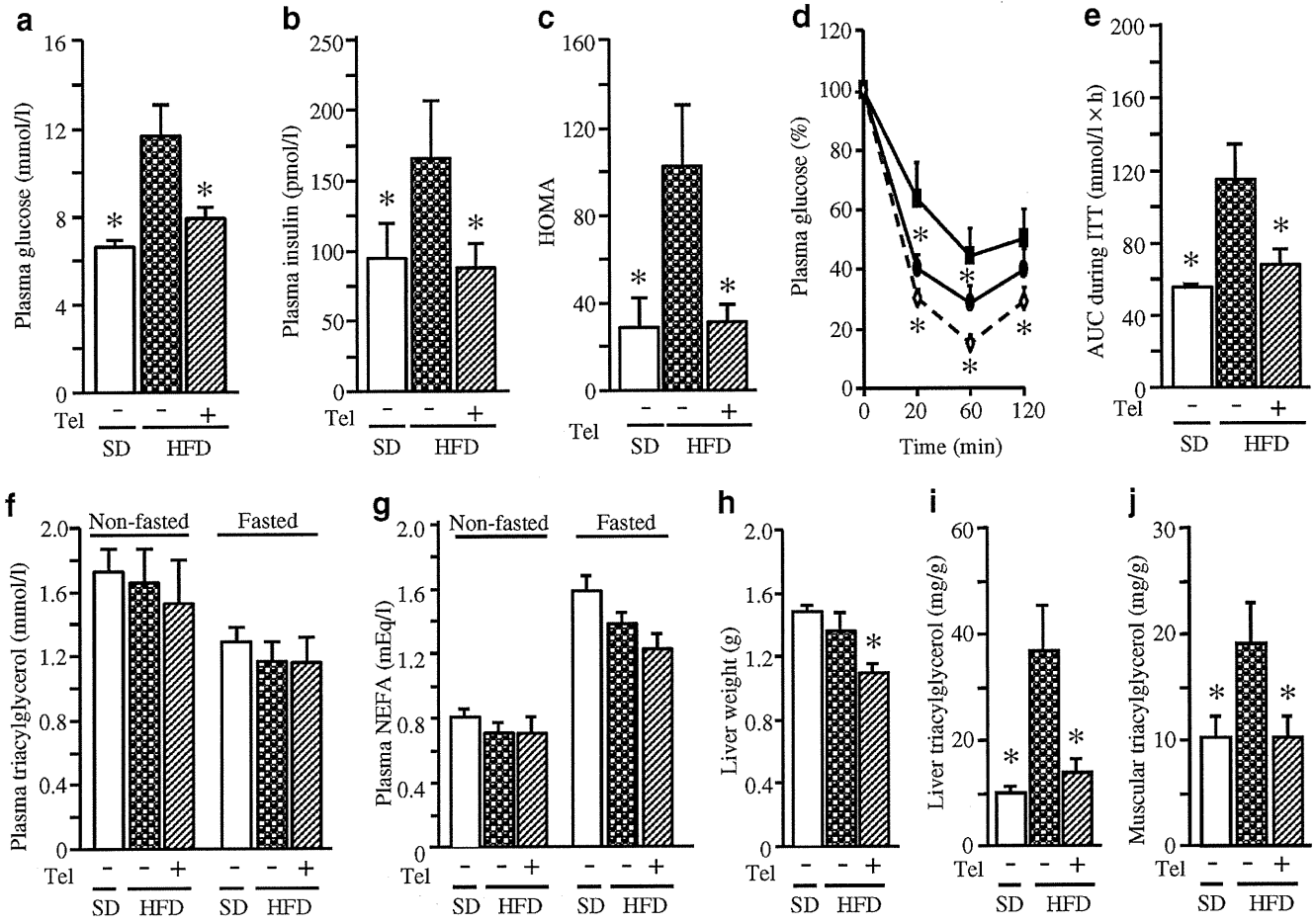

Fig. 2 Fasted (12 h) plasma concentrations of glucose (**a**) and insulin (**b**), HOMA index (**c**), plasma glucose response curve (per cent glucose change) (**d**), plasma glucose AUC following insulin challenge in ITT (Insulin 0.75 IU/kg, i.p.) (**e**), non-fasted and fasted plasma triacylglycerol concentrations (**f**), NEFA concentrations (**g**), liver weight (**h**), and triacylglycerol content of liver and skeletal muscle respectively (**i, j**) in male *Atl1*-KO mice fed a standard diet or HFD. All values are means ± SEM (n=8–10); *p<0.05 vs HFD control (Tel−). Tel−, vehicle; Tel+, telmisartan 3 mg/kg; (**d**) white diamonds, standard diet Tel−; black squares, HFD Tel−; black ovals, HFD Tel+

liver and skeletal muscle. The present findings reveal AT1-independent improvement of dietary-induced obesity, insulin resistance and fatty liver following telmisartan treatment.

Obesity is a well-established metabolic and cardiovascular risk factor. Recent advances have increased our understanding of the cellular mechanisms whereby adiposity induces adverse local and systemic effects. These include lipid accumulation in adipocytes, induction of endoplasmic reticulum and mitochondrial stress, and insulin resistance. Increased adipose tissue mass, especially in the visceral compartment, represents one of the major risk factors for development of type 2 diabetes [8]. We have recently demonstrated that telmisartan treatment improved insulin resistance and fatty liver in A-ZIP/F-1 transgenic mice lacking adipose tissue [7]. These results suggest that telmisartan may elicit its metabolic effects independently of adipose tissue. In the present study, telmisartan treatment attenuated obesity induced by HFD, a finding accompanied by improvement of insulin resistance in wild-type and *Atl1*-KO mice. Thus, the present results suggest that adipose tissue may be an alternative pathway for the insulin-sensitising effect of telmisartan.

On the other hand, an increasing body of evidence indicates that several manifestations of the metabolic syndrome and type 2 diabetes mellitus, including insulin resistance, occur as a result of overaccumulation of lipids in non-adipose tissues, such as liver and skeletal muscle [9]. A decrease in hepatic triacylglycerol pools leads to improved insulin sensitivity [10]. In the present study, HFD-feeding induced excessive lipid accumulation in liver and skeletal muscle, whereas telmisartan treatment ameliorated hepatic steatosis and muscular triacylglycerol deposition in *Atl1*-deficient mice. These results imply that attenuation of diet-induced fatty liver by telmisartan is driven by mechanisms that are independent of AT1. Thus, amelioration of lipid overaccumulation in non-adipose tissues may be an important factor associated with improved insulin action in *Atl1*-null mice following treatment with telmisartan.

In conclusion, the present findings demonstrate for the first time AT1-independent beneficial effects of telmisartan on diet-induced obesity, insulin resistance and fatty liver in mice. Activation of PPARγ might be one potential AT1-independent mechanism of action.

Acknowledgements We thank Y. Yamamoto (Kyoto University) for useful discussions during the preparation of this manuscript and W. Aini for his technical assistance during the project.

Duality of interest The authors declare that there is no duality of interest associated with this manuscript.

References

1. Cornier MA, Dabelea D, Hernandez TL et al (2008) The metabolic syndrome. Endocr Rev 29:777–822
2. Prasad A, Quyyumi AA (2004) Renin–angiotensin system and angiotensin receptor blockers in the metabolic syndrome. Circulation 110:1507–1512
3. Fujimoto M, Masuzaki H, Tanaka T et al (2004) An angiotensin II AT1 receptor antagonist, telmisartan augments glucose uptake and GLUT4 protein expression in 3T3-L1 adipocytes. FEBS Lett 576:492–497
4. Benson SC, Pershadsingh HA, Ho CI et al (2004) Identification of telmisartan as a unique angiotensin II receptor antagonist with selective PPARgamma-modulating activity. Hypertension 43:993–1002
5. Clemenz M, Frost N, Schupp M et al (2008) Liver-specific peroxisome proliferator-activated receptor alpha target gene regulation by the angiotensin type 1 receptor blocker telmisartan. Diabetes 57:1405–1413
6. Li Y, Kishimoto I, Saito Y et al (2002) Guanylyl cyclase-A inhibits angiotensin II type 1A receptor-mediated cardiac remodeling, an endogenous protective mechanism in the heart. Circulation 106:1722–1728
7. Rong X, Li Y, Ebihara K et al (2009) An adipose tissue-independent insulin-sensitizing action of telmisartan: a study in lipodystrophic mice. J Pharmacol Exp Ther 331:1096–1103
8. Bloomgarden ZT (2000) Obesity and diabetes. Diabetes Care 23:1584–1590
9. Unger RH (2002) Lipotoxic diseases. Annu Rev Med 53:319–336
10. Neschen S, Morino K, Hammond LE et al (2005) Prevention of hepatic steatosis and hepatic insulin resistance in mitochondrial acyl-CoA:glycerol-sn-3-phosphate acyltransferase 1 knockout mice. Cell Metab 2:55–65

Advance Publication by J-STAGE

Circulation Journal
Official Journal of the Japanese Circulation Society
http://www.j-circ.or.jp

Pathophysiological Remodeling of Mouse Cardiac Myocytes Expressing Dominant Negative Mutant of Neuron Restrictive Silencing Factor

Makoto Takano; Hideyuki Kinoshita; Takao Shioya; Masayuki Itoh; Kazuwa Nakao; Koichiro Kuwahara

Background: It has been previously reported that the transgenic mouse expressing the dominant negative mutant of the neuron restrictive silencing factor (dnNRSF) in the heart died from lethal arrhythmia, so the present study aimed to clarify the electrophysiological alteration of the ventricular myocyte isolated from the dnNRSF mouse.

Methods and Results: The action potential (AP) and membrane currents were recorded using the whole-cell patch-clamp method. Intracellular Ca^{2+} was measured with Indo-1AM. The AP of dnNRSF myocytes exhibited reduction of resting membrane potential, prolongation of AP duration, and frequent early afterdepolarization (EAD). The EAD was completely inhibited by SEA0400, a specific blocker of the Na^+–Ca^{2+} exchanger (NCX). The most notable alteration of membrane current was a reduction in the inward rectifier K^+ current (I_{K1}) density. In addition to re-expression of fetal type cardiac ion channels, a Na^+-permeable, late inward current was observed in a small population of dnNRSF myocytes. The diastolic intracellular Ca^{2+} concentration was also raised in dnNRSF myocytes, and spontaneous Ca^{2+} oscillation was induced by β-adrenergic stimulation.

Conclusions: In dnNRSF myocytes, the "repolarization reserve" of the AP was significantly reduced by specific alterations in membrane currents. Under these conditions, the amplitude of EAD generated by the inward NCX current might be enlarged, thereby increasing the cells' vulnerability to ventricular arrhythmia.

Key Words: Arrhythmia; Cardiac myocytes; Hypertrophy; REST/NRSF

Ventricular arrhythmias are a major cause of sudden death in patients with heart failure or cardiac hypertrophy. A characteristic genetic alteration in heart failure appears to be reactivation of fetal cardiac genes, such as atrial natriuretic peptide (ANP), α-skeletal acin, β-myosin heavy chain, and ion channels, including the hyperpolarization-activated, cyclic nucleotide-gated cation channels (I_h; Hcn2; Hcn4) and T-type Ca^{2+} channels ($I_{Ca\text{-}T}$; Cacna1h). However, the mechanisms of lethal arrhythmias still remain unclear.[1–4] We have previously reported that a transcriptional silencer, REST/NRSF (RE-1 silencing transcription factor/ neuron restrictive silencing factor) played an important role in transcriptional regulation of ANP and Hcn4 in vitro.[5,6] In accordance with this, the expressions of ANP, Hcn2, Hcn4, Cancna1h and transient receptor potential channel (Trpc1) were significantly increased in transgenic mice carrying the dominant negative mutant of REST/NRSF in their heart (dnNRSF).[7–9] The dnNRSF mice were vulnerable to ventricular arrhythmia, and started to die suddenly at approximately 8 weeks after birth without showing symptoms of pumping failure, and blockade of $I_{Ca\text{-}T}$ by efonidipine rescued them from sudden death.[7,10] In a previous study, we reported that the action potential (AP) waveform was significantly different between dnNRSF mice and their wild-type (WT) littermates.[10] Because the ionic mechanisms underlying such alteration of the AP are not clear at present, in the present study we investigated the electrophysiological properties of single ventricular myocytes isolated from dnNRSF mice, aiming to get an insight of the cellular mechanism of arrhythmias.

Methods

All experiments were approved in advance by the Animal Ethics Committee of Jichi Medical University. The investi-

Received July 6, 2010; revised manuscript received August 4, 2010; accepted August 6, 2010; released online October 30, 2010 Time for primary review: 13 days

Department of Physiology, Jichi Medical University, Tochigi (M.T., M.I.); Department of Medicine and Clinical Sciences, Graduate School of Medicine, Kyoto University, Kyoto (H.K., K.N., K.K.); and Department of Physiology, Faculty of Medicine, Saga University, Saga (T.S.), Japan

Mailing address: Makoto Takano, Department of Physiology, Jichi Medical University, 3311-1 Yakushiji, Shimotsuke, Tochigi 329-0498, Japan. E-mail: takanom@jichi.ac.jp

ISSN-1346-9843 doi:10.1253/circj.CJ-10-0652

All rights are reserved to the Japanese Circulation Society. For permissions, please e-mail: cj@j-circ.or.jp

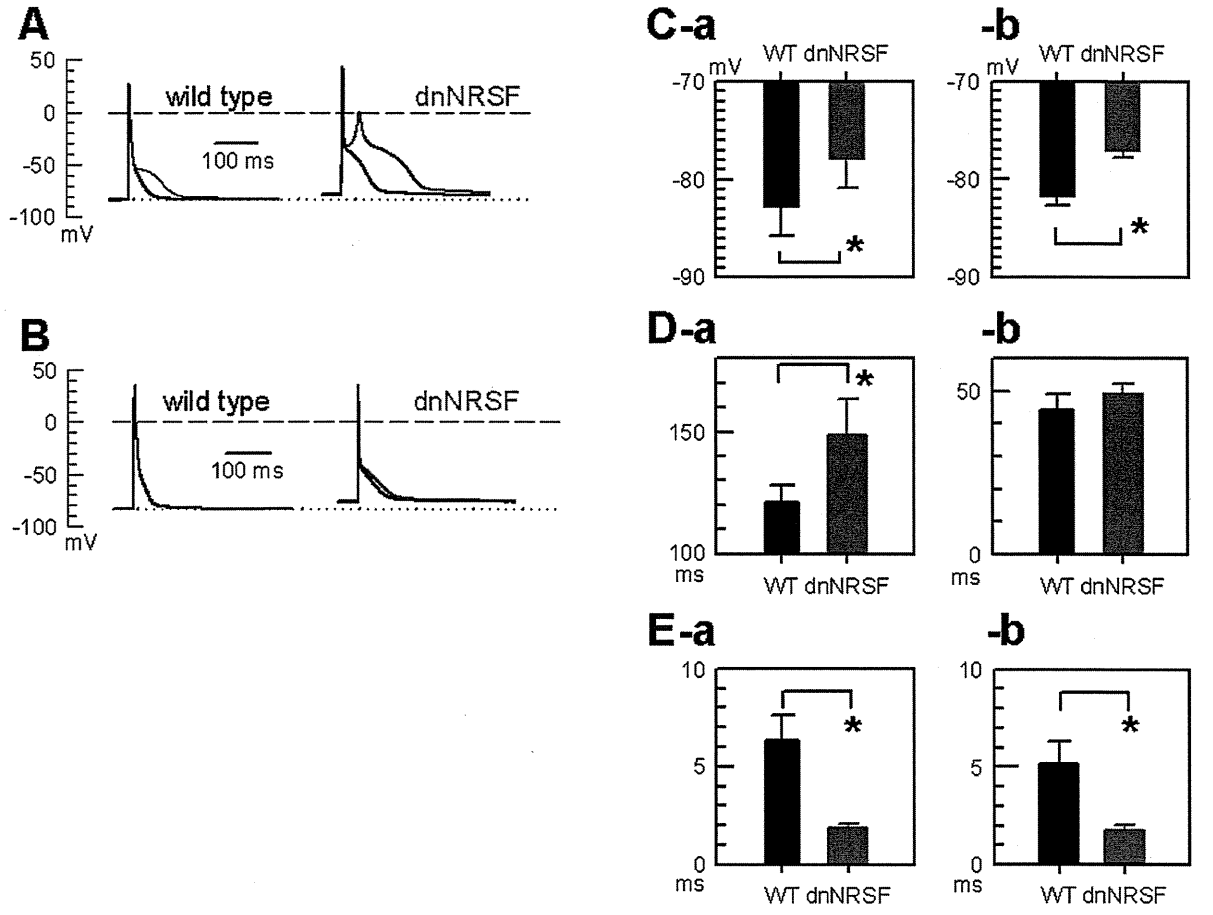

Figure 1. Action potential (AP) wave forms of ventricular myocytes isolated from wild-type (WT) and dnNRSF mice. (**A**) AP recorded using the perforated patch method. Black line, AP of WT; red line, AP of dnNRSF; blue line, APs recorded in the presence of 10 μmol/L SEA0400. The dashed line indicates 0 mV. For comparison, the resting membrane potential (RMP) of WT myocyte is shown by the dotted line. (**B**) AP recorded with the ruptured patch method. The pipette solution contained 5 mmol/L EGTA. The AP wave forms were almost superimposable in the presence (blue lines) and absence (WT, black line; dnNRSF, red line) of SEA0400. (**C-a**) Summary of RMP measured with the perforated patch method. RMP of WT was –82.7±3.1 mV (n=15); RMP of dnNRSF was significantly depolarized (–77.8±3.0 mV, n=15) ($P<0.05$). (**C-b**) RMP measured with the ruptured patch method. RMP of WT, –81.7±1.10 mV (n=15); RMP of dnNRSF, 77.1±0.8 mV (n=15) ($P<0.05$) (**D-a**) Duration of 90% AP (APD_{90}) measured with the perforated patch method. APD_{90} of dnNRSF was significantly longer (148.5±14.9 ms, n=15) than that of WT (120.8±7.0 ms, n=15) ($P<0.05$). (**D-b**) APD_{90} measured with the ruptured patch method. APD_{90} of dnNRSF is 49.7±2.8 ms (n=15); APD_{90} of WT, 44.2±4.9 ms (n=15). No statistical difference. (**E-a**) Duration of the AP measured at 0 mV (APD@0 mV) with the perforated patch method. APD@0 mV of dnNRSF was significantly shorter (1.87±0.21 ms, n=15) than that of WT (6.35±1.25 ms, n=15) ($P<0.05$). (**E-b**) APD@0 mV measured with the ruptured patch method. dnNRSF, 1.74±0.32 ms (n=15); WT, 5.16±1.11 ms (n=15) ($P<0.05$). dnNRSF, dominant negative mutant of the neuron restrictive silencing factor.

gation conformed with the Guide for the Care and Use of Laboratory Animals published by the US National Institutes of Health (NIH Publication No. 85-23, revised 1996).

Cell Isolation

Ventricular myocytes of dnNRSF mice and their WT littermates (14–16 weeks, body weight ~25 g) were obtained by a method reported previously.[11]

Composition of the Solutions

For the perforated patch experiment, the pipette solution contained (mmol/L); 110 aspartic acid, 30 KCl, 5 K_2ATP, 5 Na_2 creatine phosphate, 0.1 Na_2GTP, 1 $MgCl_2$, 10 HEPES (pH=7.2 with KOH). Amphotericin (stock solution; 30 mg/ml in DEMSO) was added to this solution (final concentration: 0.3 mg/ml). For the ruptured whole-cell patch experiments, the low-Ca^{2+} pipette solution contained: 110 aspartic acid, 30 KCl, 5 K_2ATP, 5 Na_2 creatine phosphate, 0.1 Na_2GTP, 5 EGTA, 5 HEPES (pH=7.2 with KOH). To record the Ca^{2+} and Na^+ currents, the electrode was filled with Cs^+-rich pipette solution containing: 100 CsCl, 50 NMDG, 5 MgATP, 10 EGTA, 5 HEPES (pH=7.2 with CsOH). The physiological bathing solution contained; 140 NaCl, 5.4 KCl, 0.5 $MgCl_2$, 1.8 $CaCl_2$. To record Na^+ and Ca^{2+} currents, KCl was replaced with CsCl. SEA0400 (Taisho Pharmaceutical) was dissolved in DEMSO as a stock solution (10 mmol/L).

Electrophysiology

AP and membrane current were recorded using an Axopatch200B amplifier and Digidata 1320 interface (Axon,

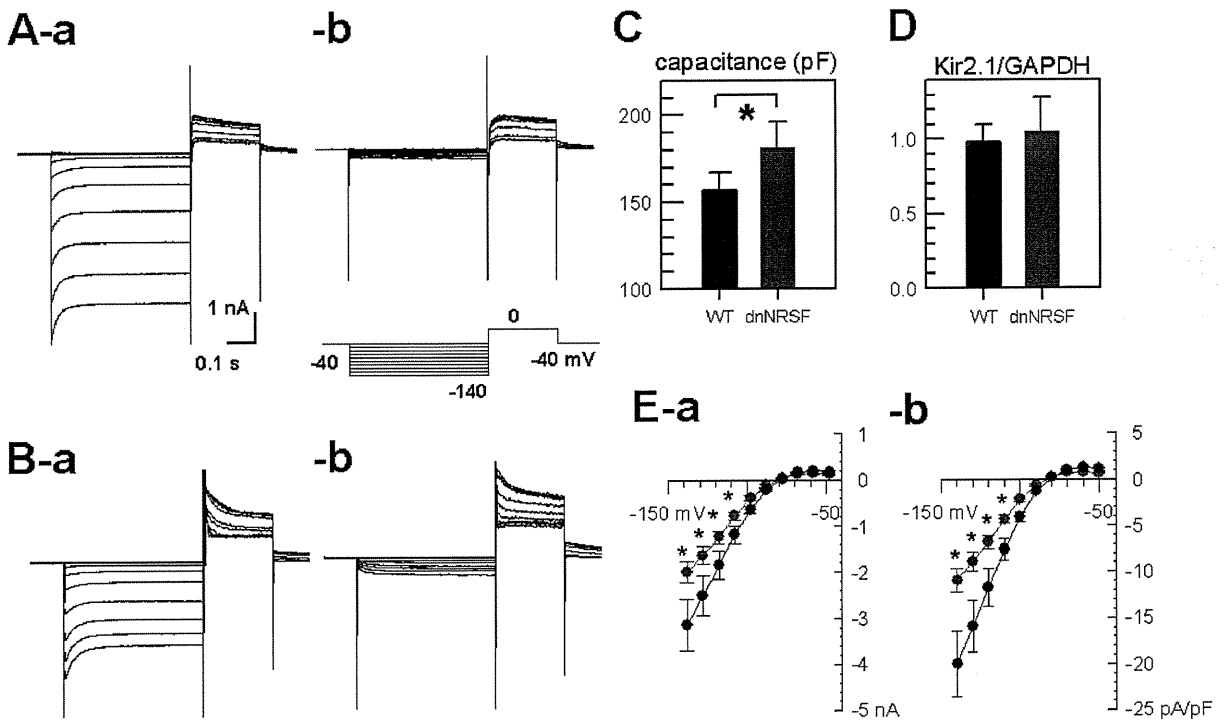

Figure 2. The reduction of I_{K1} density in dnNRSF myocytes. (**A-a**) The current traces of I_{K1} in a wild-type (WT) myocyte recorded in physiological bathing solution. (**A-b**) The family of current traces recorded in the presence of 1 mmol/L Ba^{2+}. The traces were recorded in the same myocyte as in (**A-a**). (**B-a**) I_{K1} recorded in a dnNRSF myocyte. (**B-b**) In the same myocyte shown in (**B-a**), 1 mmol/L Ba^{2+} completely inhibited I_{K1}, and disclosed the presence of I_h current at membrane potentials more negative than –80 mV. Note that the amplitude of the transient outward current at 0 mV is larger in dnNRSF. (**C**) Membrane capacitance of dnNRSF myocyte (181.1±15.3 pF, n=10) was significantly larger than that of a WT myocyte (156.8±10.2 pF, n=10) ($P<0.05$). (**D**) qPCR for Kir2.1 mRNA. Ratios of Kir2.1/GAPDH are indicated and are not statistically different between WT and dnNRSF myocytes. (**E-a**) The amplitudes of I_{K1} in a WT myocyte (black) and dnNRSF myocyte (red). The amplitude was measured at the ends of hyperpolarizing pluses. *Statistical difference (n=10, $P<0.05$). (**E-b**) The densities of I_{K1} in a WT myocyte (black) and dnNRSF myocyte (red). *Statistical difference (n=10, $P<0.05$). dnNRSF, dominant negative mutant of the neuron restrictive silencing factor; I_h, hyperpolarization-activated cation current; I_{K1}, inward rectifier K^+ current; qPCR, quantitative polymerase chain reaction.

CA, USA). The electrode resistance was 3–4 MΩ. All the experiments were carried out at 33–35°C.

Imaging

Myocytes were loaded with Indo1-AM (10 μmol/L in the bathing solution) for 15 min at room temperature. Indo-1 was excited at 340–380 nm, and the fluorescent images were captured with a CCD camera. The intensity of fluorescence was measured at 405±20 nm (F_{405}) and 480±20 nm (F_{480}) using a beam-splitter and CCD camera (AquaCosmos Double View system, Hamamatsu photonics, Hamamatsu, Japan). Fluorescent images were continuously captured at the maximum rate available in our system (1 frame per 22 ms).

qPCR Analysis

Total RNA was obtained using Trizol reagent following manufacture's instruction. Reverse transcriptase polymerase chain reaction (RT-PCR) was performed using Platinum PCR SuperMix (Invitrogen, San Diego, CA, USA). Quantitative real-time RT-PCR (qPCR) was conducted for Kir2.1 and GAPDH using predesigned TaqMan Gene Expression Assays (Applied Biosystems, Foster City, CA, USA). The reaction was performed on an ABI Prism 7700 System (Applied Biosystems). The mRNA levels of Kir2.1 were normalized to the endogenous GAPDH.

Statistical Analysis

Data are shown as mean±SEM. Statistical difference was evaluated using Student's t-test. Differences were considered significant when $P<0.05$.

Results

AP Waveform of dnNRSF Cardiac Myocytes

We first recorded the APs of single ventricular myocytes under the condition of intact intracellular Ca^{2+} transient, because it has been reported that the specific blocker of the Na^+–Ca^{2+} exchanger (NCX), SEA0400, suppresses the plateau phase of the AP in the mouse ventricle.[12] For this purpose, we used the perforated patch method. **Figure 1A** compares the AP waveform recorded in WT and dnNRSF myocytes; in the dnNRSF myocytes the resting membrane potential (RMP) was more depolarized, the AP duration (APD_{90}) was significantly prolonged, and early afterdepolarization (EAD) was observed in 37.3% (28 of 75 cells), as reported previously.[10] As shown in **Figure 1A**, SEA0400

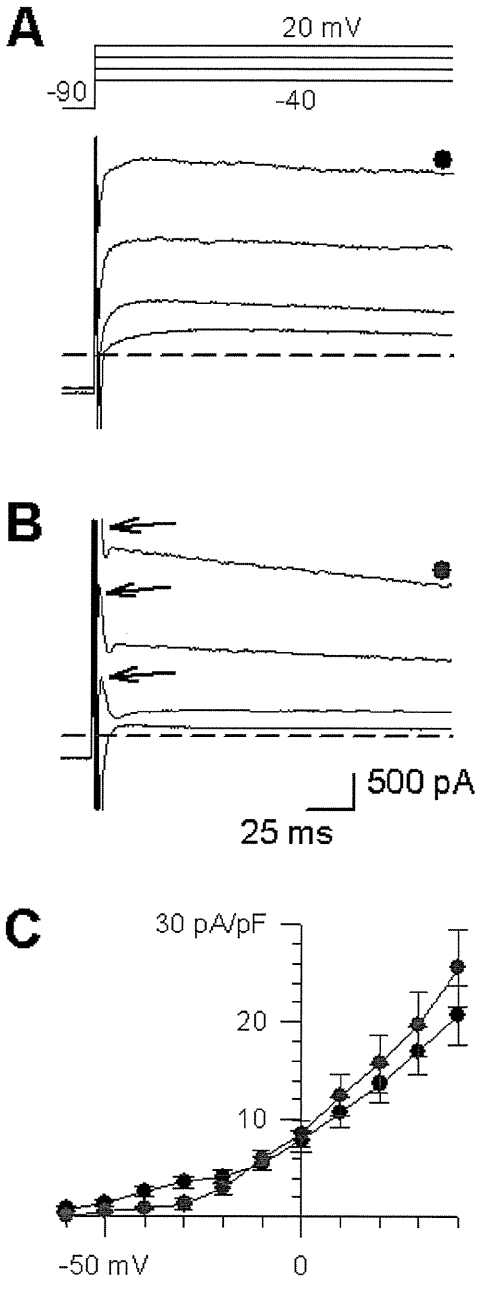

Figure 3. Comparison of the transient outward current (I_{to}) in wild-type (WT) and dnNRSF myocytes. (**A**) The family of current traces of I_{to} recorded in a WT myoycyte. The pulse protocol is shown at the top. I_{to} was recorded in physiological bathing solution. The red dashed line indicates the zero current level. The robust inward current at the onset of depolarization is the voltage-gated Na^+ current (I_{Na}). The black circle indicates the position of the measuring the quasi-steady state amplitude of I_{to}. (**B**) Two components of I_{to} recorded in dnNRSF myocytes. The blue arrows indicate the rapidly inactivating I_{to}, which was additionally activated at membrane potentials more positive than −20 mV. The red circle indicates the same as in (**A**). (**C**) IV-relationship of quasi-steady state amplitude of I_{to}. The slowly inactivating I_{to} was activated at the membrane potentials more positive than −50 mV. WT, black symbols (n=4). dnNRSF, red symbols (n=4). The current density was not statistically different. dnNRSF, dominant negative mutant of the neuron restrictive silencing factor.

shortened the plateau phase in both WT and dnNRSF myocytes. Furthermore, SEA0400 completely suppressed EADs in dnNRSF myocytes. A similar effect has been reported in dogs.[13] In contrast, when the AP was recorded using the ruptured patch method with low-Ca^{2+} pipette solution, the waveforms were almost superimposable in the presence and absence of SEA0400 (**Figure 1B**), presumably because the activity of the NCX was almost completely suppressed by chelating intracellular Ca^{2+}. Most notably, the RMP of dnNRSF myocytes was significantly more depolarized than that of WT myocytes, irrespective of the experimental conditions (**Figure 1C**). As summarized in **Figure 1D**, APD_{90} was significantly prolonged in the perforated patch experiments, whereas in the ruptured whole-cell patch experiments, APD_{90} was not statistically different between WT and dnNRSF myocytes. However, the rate of repolarization at −60 mV was significantly slower in dnNRSF myocyte, even in these experimental conditions (1.05±0.11 V/s in WT (n=15); 0.62±0.08 V/s in dnNRSF (n=15); $P<0.05$). The APD measured at 0 mV (APD@0 mV) was, however, significantly shorter in dnNRSF myocytes in both experimental conditions (**Figure 1E**).

Reduction of the Inward-Rectifier K^+ Current Density

In ventricular myocytes, the RMP is primarily determined by the inward rectifier K^+ channel (I_{K1}), close to the equilibrium potential of K^+ (E_K). In order to explore the ionic mechanisms underlying the reduced RMP in dnNRSF myocytes, we first measured the amplitude of I_{K1}. In the experiments shown in **Figures 2A,B**, the membrane current was recorded using the ruptured whole-cell patch method and low-Ca^{2+} pipette solution. The family of current traces was activated by hyperpolarizing pulses from the holding potential of −40 mV, in the presence and absence of 1 mmol/L $BaCl_2$. The amplitude of I_{K1} was defined as the Ba^{2+}-sensitive current. In dnNRSF myocytes, the hyperpolarization-activated cation current (I_h) was consistently disclosed in the presence of Ba^{2+} (**Figure 2B-b**). Upon depolarization to 0 mV, the amplitude of the transient outward current (I_{to}) appeared greater than that of the WT.

As is evident from the current–voltage (IV) relationship shown in **Figure 2E-a**, the amplitude of I_{K1} was significantly smaller in dnNRSF myocytes. Furthermore, the cellular capacitance was significantly larger in dnNRSF myocytes (**Figure 2C**). As a consequence, the density of I_{K1} was remarkably reduced in dnNRSF myocytes; the density of the inward I_{K1} at −140 mV was 56.0% and the density of the outward I_{K1} at −60 mV was 55.1% of WT myocytes, showing no voltage dependence in the inhibition (**Figure 2E-b**). The magnitude of the reduction of I_{K1} density appeared to be in good agreement with the reduction of dV/dt measured at −60 mV. In cardiac myocytes, Kir2.1 is a major molecular component of the I_{K1} channel, so we compared the amount of Kir2.1 mRNA using qPCR. However, there was no significant difference in the expression level of Kir2.1 (**Figure 2D**), which suggests that the reduction in I_{K1} density was caused by post-transcriptional mechanisms.

Transient Outward Current It has been reported that the voltage-gated outward currents, including I_{to}, play a major role in the modification of AP morphology in mouse cardiac myocytes.[14] We compared the voltage-gated outward currents recorded in WT- and dnNRSF myocytes (**Figure 3**). In this experiment, the membrane current was activated from the holding potential of −90 mV in the physiological bathing solution. Therefore, robust activation of Na^+ current (I_{Na})

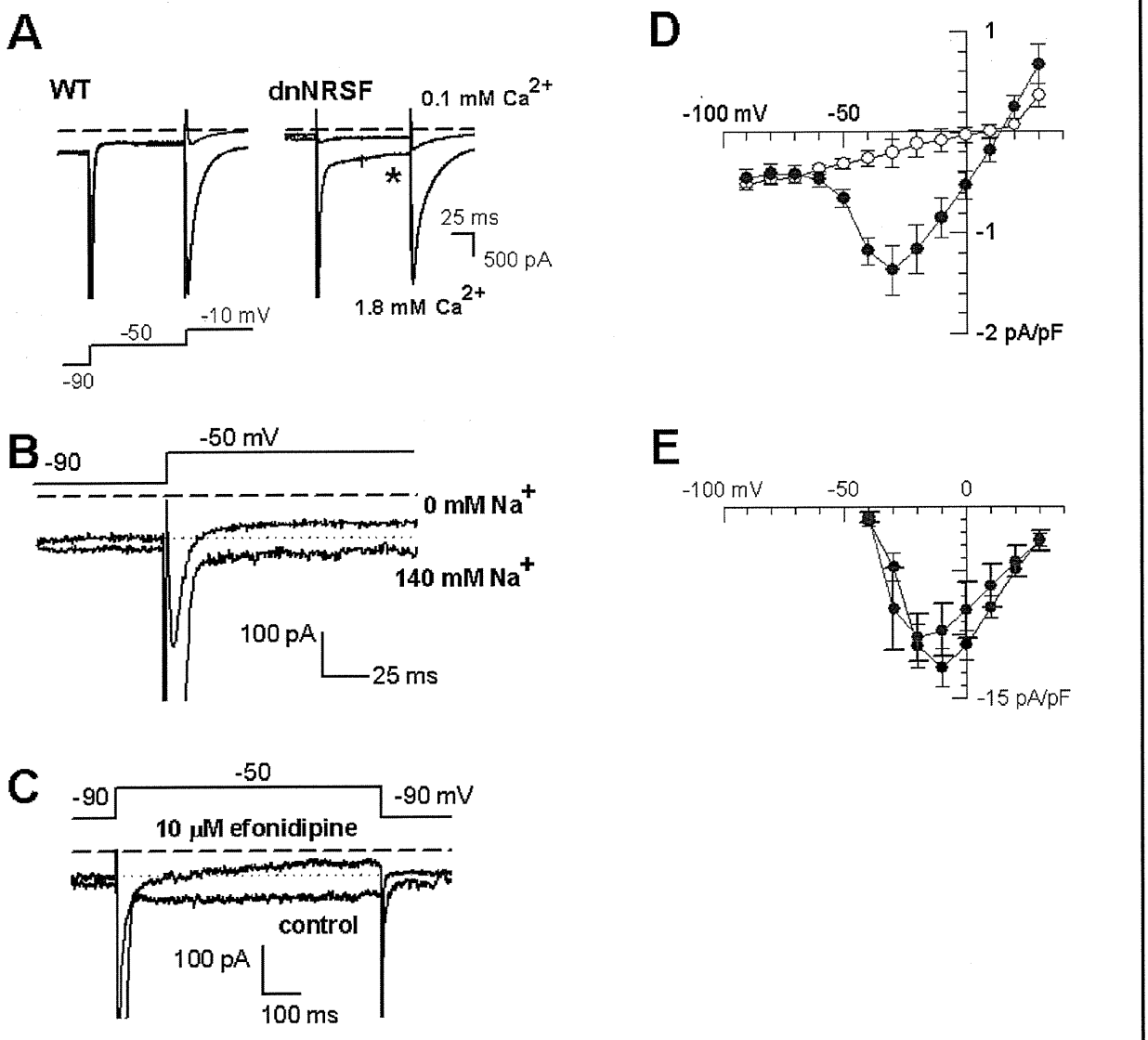

Figure 4. Na^+-permeable, sustained inward current in dnNRSF myocytes. (**A**) Voltage-gated inward currents were activated by 2-step pulses. In the WT myocyte, no inward current was activated at –50 mV. $I_{Ca\text{-}L}$ was activated at –10 mV. In the dnNRSF myocyte, late inward current was observed at the end of voltage stepping to –50 mV. When the Ca^{2+} concentration of the bathing solution was reduced from 1.8 mmol/L (black lines) to 0.1 mmol/L (red lines), the amplitude of the late inward current was increased (*). (**B**) Na^+-sensitive nature of the late inward current activated at –50 mV. The current traces were recorded in the presence (black line) and absence (blue line) of 140 mmol/L Na^+. The Ca^{2+} concentration was 1.8 mmol/L. The dashed line indicates the zero current level, and the red dotted line is the mean holding current at –90 mV. Note that late inward current was observed at –50 mV in the 140 mmol/L Na^+ bathing solution. In Na^+-free conditions, $I_{Ca\text{-}T}$ was disclosed at the onset of the voltage stepping at –50 mV, whereas the late inward current was completely suppressed. (**C**) The late inward current activated by long voltage pulse (500 ms). The bathing solution contained 1.8 mmol/L Ca^{2+} and 140 mmol/L Na^+. The dashed line and red dotted line indicate the same as in (**B**). 10 μmol/L efonidipine completely inhibited the late inward current. (**D**) IV-relationship of the late inward current. The current amplitudes were measured at the end of the 1st voltage pulse shown in the inset of (**A**). Red symbols, 0.1 mmol/L Ca^{2+}/140 mmol/L Na^+. White symbols, 1.8 mmol/L Ca^{2+}/0 mmol/L Na^+ (n=8). (**E**) IV-relationship of $I_{Ca\text{-}L}$. Red symbols, dnNRSF (n=8); black symbols, WT (n=8). The peak amplitude of $I_{Ca\text{-}L}$ was measured using the 2-step pulse protocol shown in (**A**). dnNRSF, dominant negative mutant of the neuron restrictive silencing factor; $I_{Ca\text{-}L}$, L-type Ca^{2+} current; WT, wild-type.

and L-type Ca^{2+} current ($I_{Ca\text{-}L}$) overlapped during the activation phase of the outward currents, and interfered with the measurement of the peak amplitude of I_{to}. We therefore compared the amplitudes of quasi-steady state currents of I_{to}. The densities of the quasi-steady state currents were not statistically different at any of the membrane potentials examined (**Figure 3B**).

However, at the onset of depolarization pulses, rapidly inactivating I_{to} was observed in dnNRSF myocytes at membrane potentials more positive than –20 mV (**Figure 3B**). The molecular entities of this rapid I_{to} remain unclear at present. An outward tail current of I_h may be partly involved. Because the time course of inactivation was extremely rapid, this component seemed completely inactivated at the quasi-

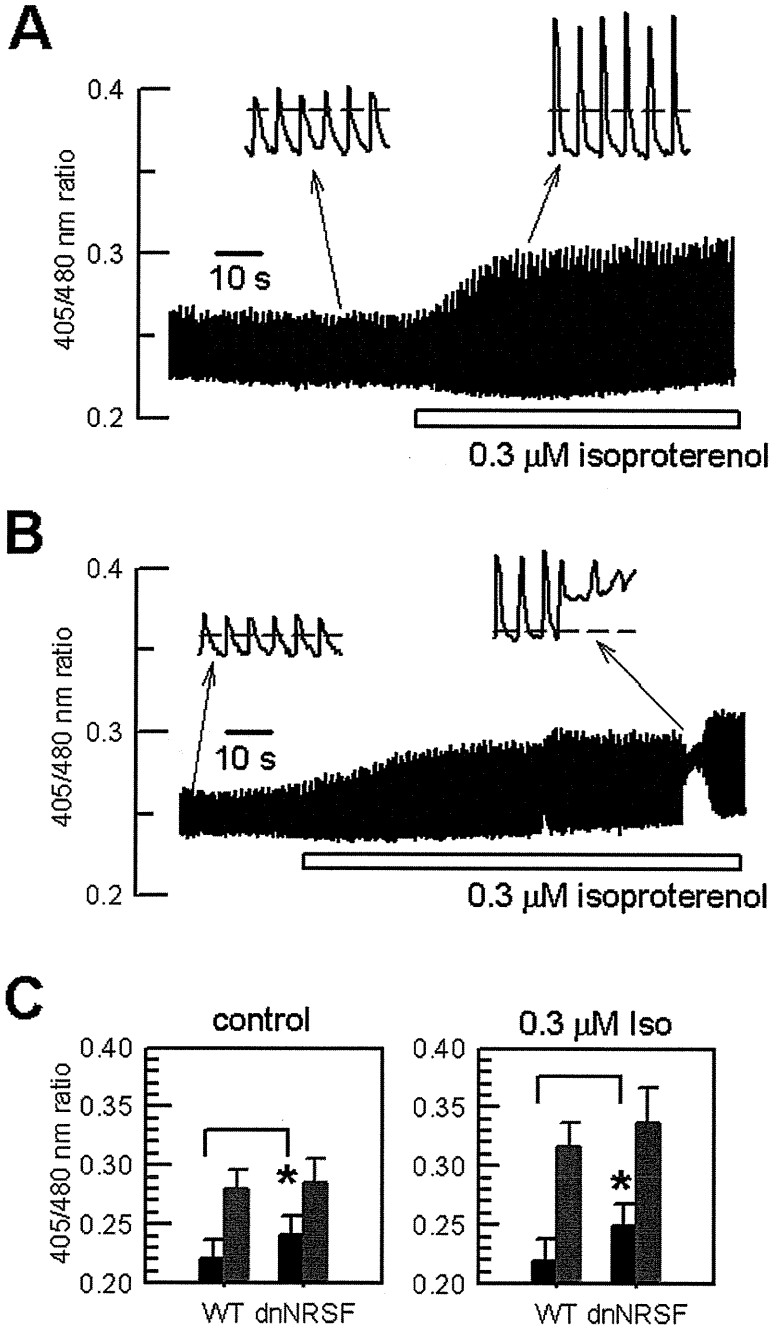

Figure 5. Intracellular Ca^{2+} transient measured with Indo-1AM. The abscissa indicates the ratio of fluorescent intensity measured at 405 nm and 480 nm ($F_{405/480}$). The Indo-1AM loaded myocytes were perfused with physiological bathing solution kept at 33–35°C, and field-stimulated at 2 Hz. (**A**) Continuous trace of $F_{405/480}$ recorded in WT myocytes. The application of 0.3 μmol/L isoproterenol is indicated by the white bar. The inset shows the expanded traces of $F_{405/480}$ for 3 s, in the presence and absence of isoproterenol. The dashed line indicates $F_{405/480}$=0.25. (**B**) $F_{405/480}$ trace measured in dnNRSF myocytes. After the application of 0.3 μmol/L isoproterenol, diastolic $F_{405/480}$ slightly increased, followed by spontaneous oscillation. The inset shows the expanded trace at the onset of spontaneous oscillation for 3 s. The dashed line indicates $F_{405/480}$=0.25. (**C**) Summary of $F_{405/480}$ measured in WT and dnNRSF cardiac myocytes (n=15, $P<0.05$). The black bars indicate diastolic $F_{405/480}$, and the red bars, systolic $F_{405/480}$. In both the presence and absence of isoproterenol, diastolic $F_{405/480}$ was significantly higher in dnNRSF (n=15, $P<0.05$). dnNRSF, dominant negative mutant of the neuron restrictive silencing factor; WT, wild-type.

steady state in both WT and dnNRSF (**Figures 3A,B**). As shown in **Figure 1**, ADP@0 mV was shorter in dnNRSF myocytes, presumably because the amplitude of the rapid I_{to} was larger in dnNRSF myocytes.

Na^+-Permeable Late Current It has been reported that the late Na^+ current is increased in myocytes from a heart failure model.[15,16] Therefore, we explored the possibility that Na^+ conductance might contribute to the reduced RMP in dnNRSF. In the experiments shown in **Figure 4A**, we activated the voltage-gated I_{Na} and $I_{Ca\text{-}L}$ using 2-step voltage pulses. The K^+ conductance were completely suppressed by using a Cs^+-rich pipette solution and by replacing extracellular K^+ with Cs^+. In 8 of 40 myocytes isolated from dnNRSF, a sustained inward component was observed at the end of voltage stepping to −50 mV. When the extracellular Ca^{2+} concentration was reduced from 1.8 mmol/L to 0.1 mmol/L, the sustained inward component at −50 mV was clearly enlarged. However, such a sustained inward component was never recorded in WT myocytes.

In order to clarify the ionic selectivity of this component, dnNRSF myocytes were perfused with Na^+-free, 1.8 mmol/L Ca^{2+} solution. As shown in **Figure 4B**, the inward current jump at −50 mV in 140 mmol/L Na^+ solution was completely suppressed, and activation of the $I_{Ca\text{-}T}$ followed by an outward current jump was disclosed. $I_{Ca\text{-}T}$ was recorded in a small population of dnNRSF myocytes (5 of 75). Unexpect-

edly, we found that this inward current jump at −50 mV was sensitive to calcium-channel blockers. As shown in **Figure 4C**, 10 μmol/L efonidipine almost completely inhibited the Na^+-permeable, sustained inward current (I_{st}) at −50 mV. **Figure 4D** shows the IV relationship of I_{st} measured at the end of the depolarizing pulse in 140 mmol/L Na^+/0.1 mmol/L Ca^{2+} solution, and in Na^+-free/0.1 mmol/L Ca^{2+} solution. I_{st} was activated at membrane potentials more positive than −60 mV, and the reversal potential was between 10 and 20 mV.

The amplitude of $I_{Ca\text{-}L}$ also affects the morphology of the AP of cardiac myocytes. We therefore compared the amplitude of $I_{Ca\text{-}L}$ activated by a 2-step pulse protocol (**Figure 4A**). As is evident from the IV-relationship shown in **Figure 4E**, the density of $I_{Ca\text{-}L}$ was not significantly different between WT and dnNRSF myocytes at any of the membrane potentials examined. However, the profile of the IV-relationship was slightly different: in WT myocytes, the peak of the IV relationship was at −10 mV, whereas in dnNRSF myocytes, it was at −20 mV.

Intracellular Ca^{2+} Transient

Alteration of intracellular Ca^{2+} handling as part of the remodeling in the hypertrophied or failing heart is well known.[17] As shown in **Figure 1**, the EAD and prolonged APD observed in dnNRSF myocytes were completely suppressed by a specific blocker of the NCX. Therefore, it appears reasonable to expect that intracellular Ca^{2+} handling is also altered in dnNRSF myocytes. We compared the intracellular Ca^{2+} transient of intact myocytes isolated from WT and dnNRSF (**Figure 5**). The myocytes were loaded with Indo1-AM, and the ratio of fluorescent intensity was measured at 405 nm and 480 nm ($F_{405/480}$). The Ca^{2+} transient of myocytes was induced by field stimulation at 2 Hz. As summarized in **Figure 5C**, diastolic $F_{405/480}$ was 0.22±0.02 in WT myocytes (n=15). In dnNRSF myocytes, the diastolic intracellular Ca^{2+} concentration ($[Ca^{2+}]_i$) was significantly higher; $F_{405/480}$ was 0.24±0.02 (n=15) ($P<0.05$). In contrast, systolic $F_{405/480}$ was not significantly different between WT (0.28±0.02, n=15) and dnNRSF myocytes (0.29±0.02, n=15).

Adrenergic stimulation seemed to trigger abnormal electrical activity in dnNRSF myocytes, as reported previously.[10] We therefore compared the effects of 0.3 μmol/L isoproterenol on the Ca^{2+} transient. As shown in **Figure 5A**, the peak $[Ca^{2+}]_i$ of WT myocytes increased promptly after application of isoproterenol, and reached a steady level within approximately 40 s. The diastolic $[Ca^{2+}]_i$ decreased slightly but transiently from the control level. In dnNRSF myocytes, the systolic $[Ca^{2+}]_i$ was also increased by isoproterenol, demonstrating that the response to β-adrenergic stimulation was retained. However, diastolic $[Ca^{2+}]_i$ slowly increased after the application of isoproterenol and spontaneous $[Ca^{2+}]_i$ oscillation was induced (**Figure 5B inset**). Spontaneous $[Ca^{2+}]_i$ oscillation presumably activates the Ca^{2+}-dependent inward current carried by the NCX, giving rise to the abnormal electrical activity of dnNRSF myocytes.[10]

In our experimental system, the maximal rate of image capture was 1 frame per 22 ms. Because of this limitation, the recording of the Ca^{2+} transient was discontinuous; we could obtain only 22 data points with 22-ms interval in 1 cycle (500 ms) of field stimulation. Therefore, it was practically difficult to evaluate the precise values of the time-to-peak and the half relaxation time of the $[Ca^{2+}]_i$ transient during the AP of mouse cardiac myocytes.

Discussion

In animal models of the hypertrophied or failing heart, physiological remodeling so far reported may be summarized as follows. First, alteration of intracellular Ca^{2+} handling, such as Ca^{2+} leak from the sarcoplasmic reticulum and downregulation of Ca^{2+}-ATPase. Second, downregulation of the "repolarization reserve", such as decreased outward currents and/or increased inward currents. Third, re-expression of fetal-type genes, such as contractile proteins and ion channels.[1-4] Of these physiological remodeling processes, it has been suggested that transcriptional repressor REST/NRSF primarily plays a role in the regulation of fetal cardiac genes. In the heart, REST/NRSF represses the transcription of fetal cardiac genes in mature animals, and the hypertrophic stimulation appears to release, at least in part, the transcriptional repression by REST/NRSF.[18]

In the present study, we have demonstrated that inhibition of the REST/NRSF function significantly downregulated the "repolarization reverse" of ventricular myocytes, in addition to the re-expression of fetal-type ion channels such as I_h and $I_{Ca\text{-}T}$. The density of I_{K1} was remarkably reduced, in spite of the mRNA level of Kir2.1 being unchanged. The mechanisms underlying the reduction in I_{K1} density is not clear at present. It has been reported that elevation of diastolic $[Ca^{2+}]_i$ reduces I_{K1} density in rat hypertrophied myocytes, via protein kinase C (PKC)-dependent and PKC-independent pathways.[19] Therefore, it might be speculated that in the hypertrophied heart a series of physiological changes (eg, reduction of I_{K1} density, depolarization of RMP, reduction of the driving force of NCX, elevation of diastolic $[Ca^{2+}]_i$) could form a vicious spiral. Because diastolic $[Ca^{2+}]_i$ was also elevated in the dnNRSF myocytes (**Figure 4**), similar mechanisms might be involved in the reduction of I_{K1} density.

I_{to} is an important determinant of AP morphology in mouse cardiac myocytes, and a decrease in the I_{to} density should also reduce the "repolarization reserve".[14] In the present study, the density of the slow component of I_{to} was not decreased in dnNRSF myocytes. In contrast, the density of rapidly inactivating I_{to} was increased. Because rapid I_{to} was only activated at membrane potentials >−20 mV, and was completely inactivated within 5 ms, this component might modify only the duration of overshoot, without affecting the duration of the plateau phase at −40 mV. Vice versa, the activation of rapid I_{to} might increase the driving force of $I_{Ca\text{-}L}$, giving rise to a transient increase of Ca^{2+} influx.

As a mechanism of the reduction of the "repolarization reserve" and the generation of EAD in the hypertrophied heart, the late I_{Na} is now receiving much attention.[15,16] The late I_{Na} (ie, delayed inactivation of I_{Na}) seems to be regulated by calmodulin kinase II (CaMKII).[20] In dnNRSF myocytes, it appears reasonable to expect that I_{Na} was modified by CaMKII, which was activated by the elevation of diastolic $[Ca^{2+}]_i$. In fact, the Na^+-permeable, sustained I_{st} was observed in a small population of dnNRSF myocytes. Increase of Na^+ influx through I_{st} and I_h is anticipated in dnNRSF myocytes. Alteration of Na^+ homeostasis may reduce of the driving force of the NCX, thereby increasing $[Ca^{2+}]_i$.[21]

It has been reported that late I_{Na} is sensitive to ranolazine.[16] Although we have not yet examined the effect of ranolazine on I_{st} in dnNRSF myocytes, this current might not be delayed inactivation of I_{Na}, because I_{st} in dnNRSF myocytes was sensitive to calcium-channel blocker (**Figure 3C**), showing a similarity to the sustained inward current reported in the sino-atrial node.[22] We have previously reported that

efonidipine rescued the lethal arrhythmia of dnNRSF mice.[10] Therefore, in addition to $I_{Ca\text{-}L}$ and $I_{Ca\text{-}T}$, I_{st} might be an important pharmacological target in dnNRSF myocytes.

Study Limitations

It still remains unclear which of the primary genetic alternations caused by dnNRSF initiates the physiological remodeling series. Because diastolic $[Ca^{2+}]_i$ was elevated in dnNRSF myocytes, Ca^{2+}-dependent genetic alterations might have subsequently occurred.[23] It has been recently reported that Cav3.2 (Cacna1h) is required for cardiac hypertrophy induced by pressure overload.[24] Likewise, crossbreeding of dnNRSF mice with transgenic mice lacking the target genes of REST/NRSF might provide a clue.

Conclusion

We found that RMP was reduced, and APD_{90} prolonged in dnNRSF myocytes. These changes were caused by a reduction in the "repolarization reserve", which in turn was caused by reduced I_{K1} density and the emergence of a Na^+-permeable, late inward current. The diastolic $[Ca^{2+}]_i$ was elevated, and spontaneous oscillation of $[Ca^{2+}]_i$ was induced by β-adrenergic stimulation. Under these conditions, the amplitude of EAD generated by the inward NCX current might be increased, thereby increasing the vulnerability to ventricular arrhythmia.

Acknowledgment

We appreciate the contribution of Akiko Kuratomi in the early stage of this work, and thank Taisho Pharmaceutical Co Ltd for the generous gift of SEA0400. This work was supported by grants-in-aid for Scientific Research from the Ministry of Education, Culture, Sports, Science and Technology of Japan (#16650088, #17659063), and the Vehicle Racing Commemorative Foundation.

References

1. Nattel S, Khairy P, Schram G. Arrhythmogenic ionic remodeling: Adaptive response with maladaptive consequences. *Trends Cardiovasc Med* 2001; **11:** 295–301.
2. Tomaselli GF, Zipes DP. What causes sudden death in heart failure? *Circ Res* 2004; **95:** 754–763.
3. Pogwizd SM, Bers DM. Cellular basis of triggered arrhythmias in heart failure. *Trends Cardiovasc Med* 2004; **14:** 61–66.
4. Koyama T, Ono K, Watanabe H, Ohba T, Murakami M, Iino K, et al. Molecular and electrical remodeling of L- and T-type Ca^{2+} channels in rat atrium with monocrotaline-induced pulmonary hypertension. *Circ J* 2009; **73:** 256–263.
5. Kuwahara K, Saito Y, Ogawa E, Takahashi N, Nakagawa Y, Naruse Y, et al. The neuron-restrictive silencer element-neuron-restrictive silencer factor system regulates basal and endothelin 1-inducible atrial natriuretic peptide gene expression in ventricular myocytes. *Mol Cell Biol* 2001; **21:** 2085–2097.
6. Kuratomi S, Kuratomi A, Kuwabara K, Ishii TM, Nakao K, Saito Y, et al. NRSF regulates the developmental and hypertrophic changes of HCN4 transcription in rat cardiac myocytes. *Biochem Biophys Res Commun* 2007; **353:** 67–73.
7. Kuwahara K, Saito Y, Takano M, Arai Y, Yasuno S, Nakagawa Y, et al. NRSF regulates the fetal cardiac gene program and maintains normal cardiac structure and function. *EMBO J* 2003; **22:** 6310–6321.
8. Ohba T, Watanabe H, Takahashi Y, Suzuki T, Miyoshi I, Nakayama S, et al. Regulatory role of neuron-restrictive silencing factor in expression of TRPC1. *Biochem Biophys Res Commun* 2006; **351:** 764–770.
9. Watanabe H, Murakami M, Ohba T, Ono K, Ito H. The pathological role of transient receptor potential channels in heart disease. *Circ J* 2009; **73:** 419–427.
10. Kinoshita H, Kuwahara K, Takano M, Arai Y, Kuwabara Y, Yasuno S, et al. T-type Ca^{2+} channel blockade prevents sudden death in mice with heart failure. *Circulation* 2009; **120:** 743–752.
11. Shioya T. A simple technique for isolating healthy heart cells from mouse models. *J Physiol Sci* 2007; **57:** 327–335.
12. Tanaka H, Namekawa I, Takeda K, Kazama A, Shimizu Y, Moriwaki R, et al. Unique excitation-contraction characteristics of mouse myocardium as revealed by SEA0400, a specific inhibitor of Na^+-Ca^{2+} exchanger. *Naunyn-Schmiederbers's Arch Pharmacol* 2005; **371:** 526–534.
13. Nagy ZA, Toth A, Biliczki P, Acsai K, Banyasz T, Nanasi P, et al. Selective inhibition of sodium-calcium exchanger by SEA0400 decreases early and delayed after depolarization in canine heart. *Br J Pharmacol* 2004; **143:** 827–831.
14. Odening KE, Nerbonne JM, Bode C, Zehender M, Brunner M. In vivo effect of a dominant negative Kv4.2 loss-of-function mutation eliminating $I_{to,f}$ on atrial refratoriness and atrial fibrillation in mice. *Circ J* 2009; **73:** 461–467.
15. Valdivia CR, Chu WW, Pu J, Foell JD, Haworth RA, Wolff MR, et al. Increased late sodium current in myocytes from a canine heart failure model and from failing human heart. *J Mol Cell Cardiol* 2005; **38:** 475–483.
16. Eckhardt LL, Teelin TC, January CT. Is ranolazine an antiarrhythmic drug? *Am J Physiol* 2008; **294:** H1989–H1991.
17. Eisner DA, Kshimura T, Venetucci LA, Trafford AW. From the ryanodine receptor to cardiac arrhythmias. *Circ J* 2009; **73:** 1561–1567.
18. Nakagawa Y, Kuwahara K, Harada M, Takahashi N, Yasuno S, Adachi Y, et al. Class II HDACs mediate CaMK-dependent signaling to NRSF in ventricular myocytes. *J Mol Cell Cardiol* 2006; **41:** 1010–1022.
19. Fauconnier J, Lacampagne A, Rauzier JM, Vassort G, Richard S. Ca^{2+}-dependent reduction of I_{K1} in rat ventricular cells: A novel paradigm for arrhythmia in heart failure? *Cardiovasc Res* 2005; **68:** 204–212.
20. Xie LH, Chen F, Karaguenzian HS, Weiss JN. Oxidative stress induced afterdepolarizations and calmodulin kinase II signaling. *Circ Res* 2008; **104:** 79–86.
21. Bers DM, Despa S. Cardiac myocytes Ca^{2+} and Na^+ regulation in normal and failing hearts. *J Pharmacol Sci* 2006; **100:** 315–322.
22. Cho HS, Takano M, Noma A. The electrophysiological properties of spontaneously beating pacemaker cells isolated from mouse sinoatrial node. *J Physiol* 2003; **550:** 169–180.
23. Heineke J, Molkentin JD. Regulation of cardiac hypertrophy by intracellular signaling pathways. *Nat Rev Mol Cell Biol* 2006; **7:** 589–600.
24. Chiang CS, Huang CH, Chieng H, Chang YT, Chang D, Chen JJ, et al. The Cav3.2 T-type Ca^{2+} channel is required for pressure overload-induced cardiac hypertrophy in mice. *Circ Res* 2009; **104:** 522–530.

MOLECULAR AND CELLULAR BIOLOGY, Sept. 2010, p. 4134–4148 Vol. 30, No. 17
0270-7306/10/$12.00 doi:10.1128/MCB.00154-10
Copyright © 2010, American Society for Microbiology. All Rights Reserved.

Myocardin-Related Transcription Factor A Is a Common Mediator of Mechanical Stress- and Neurohumoral Stimulation-Induced Cardiac Hypertrophic Signaling Leading to Activation of Brain Natriuretic Peptide Gene Expression▽†

Koichiro Kuwahara,* Hideyuki Kinoshita, Yoshihiro Kuwabara, Yasuaki Nakagawa, Satoru Usami, Takeya Minami, Yuko Yamada, Masataka Fujiwara, and Kazuwa Nakao

Department of Medicine and Clinical Science, Kyoto Graduate School of Medicine, 54 Kawaracho Shogoin Sakyo-ku, Kyoto, Japan 606-8507

Received 7 February 2010/Returned for modification 2 April 2010/Accepted 28 June 2010

Subjecting cardiomyocytes to mechanical stress or neurohumoral stimulation causes cardiac hypertrophy characterized in part by reactivation of the fetal cardiac gene program. Here we demonstrate a new common mechanism by which these stimuli are transduced to a signal activating the hypertrophic gene program. Mechanically stretching cardiomyocytes induced nuclear accumulation of myocardin-related transcription factor A (MRTF-A), a coactivator of serum response factor (SRF), in a Rho- and actin dynamics-dependent manner. Expression of brain natriuretic peptide (BNP) and other SRF-dependent fetal cardiac genes in response to acute mechanical stress was blunted in mice lacking MRTF-A. Hypertrophic responses to chronic pressure overload were also significantly attenuated in mice lacking MRTF-A. Mutation of a newly identified, conserved and functional SRF-binding site within the BNP promoter, or knockdown of MRTF-A, reduced the responsiveness of the BNP promoter to mechanical stretch. Nuclear translocation of MRTF-A was also involved in endothelin-1- and angiotensin-II-induced activation of the BNP promoter. Moreover, mice lacking MRTF-A showed significantly weaker hypertrophic responses to chronic angiotensin II infusion than wild-type mice. Collectively, these findings point to nuclear translocation of MRTF-A as a novel signaling mechanism mediating both mechanical stretch- and neurohumoral stimulation-induced BNP gene expression and hypertrophic responses in cardiac myocytes.

Hemodynamic overload, a combination of mechanical stress and neurohumoral stimulation, induces a hypertrophic response characterized in part by reactivation of the fetal gene program in cardiac myocytes (4, 15, 25, 45, 58). Though cardiac hypertrophy initially serves as an adaptive response to increased cardiac output, when sustained it leads to cardiac decompensation and heart failure, which is now a leading cause of morbidity and mortality around the world. Thus, elucidation of the molecular mechanisms underlying the development and progression of cardiac hypertrophy is an important issue when considering therapeutic intervention. To delineate the molecular pathways involved in the hypertrophic response to mechanical stress, *in vitro* stretching devices have been developed that enable stretch stress to be applied to cultured cardiac myocytes (51, 62). Using these devices, it was revealed that mechanical stress activates several signal transduction pathways involving mitogen-activated protein kinases (MAPKs), protein kinase C (PKC), Jak-STAT, and small G proteins (e.g., Rho, Rac, and Ras) in cultured cardiac myocytes (1, 16, 27, 47, 48, 51, 62). How these signaling molecules transduce mechanical stretch to a signal activating a set of transcription factors and ultimately the hypertrophic gene program, however, remains unclear.

In addition to mechanical stress, neurohumoral stimulation is also known to be a pivotal contributor to the chronic remodeling process in hearts (45). Angiotensin II (AngII), phenylephrine, and endothelin 1 (ET-1), which all act through G-protein-coupled receptors, have all been shown to induce cardiac hypertrophy. Clinical evidence showing the favorable effects of blocking AngII signaling on the course of heart failure and the ability of AngII blockade to repress cardiac hypertrophy supports the notion that neurohumoral factors play an important role in pathological cardiac remodeling (8). Among the variety of intracellular signaling molecules that have been shown to be activated following mechanical stretch or neurohumoral stimulation, Rho family small GTPases, especially Rho A and Rac1, have been highlighted as important regulators for cardiac hypertrophy (5, 24). The precise downstream mechanisms by which Rho GTPases activate the hypertrophic gene program remain obscure, however.

Serum response factor (SRF) is a MADS box transcription factor that regulates the expression of immediate-early genes and muscle-specific genes by binding to a conserved sequence [$CC(A/T)_6GG$] known as the CArG box or serum response element. Moreover, several findings have confirmed the involvement of SRF in the induction of a subset of cardiac genes during adverse cardiac remodeling (23, 32, 34, 36, 57). Targeted deletion of SRF in the developing heart results in lethal cardiac defects, with reduced expression of many cardiac-spe-

* Corresponding author. Mailing address: Department of Medicine and Clinical Science, Kyoto University Graduate School of Medicine, 54 Kawaracho, Shogoin, Sakyo-ku, Kyoto 606-8507, Japan. Phone: 81-75-751-4287. Fax:. 81-75-771-9452. E-mail: kuwa@kuhp.kyoto-u.ac.jp.

† Supplemental material for this article may be found at http://mcb.asm.org/.

▽ Published ahead of print on 6 July 2010.

cific genes (33, 49). In addition, overexpression of SRF in the postnatal heart leads to cardiomyopathy with increased fetal cardiac gene expression (63), while conditional deletion of SRF in isolated neonatal cardiac myocytes results in reduced expression of hypertrophic genes (43). Several fetal cardiac genes, including atrial natriuretic peptide (ANP), skeletal α-actin, smooth muscle α-actin, and smooth muscle 22α (SM22α), have been shown to contain a functionally important CArG box in their upstream transcription control region (53, 57). At least two signaling pathways are known to modulate SRF activity, one involving the phosphorylation of ternary complex factors in Ets domain family proteins and another controlled by Rho family small GTPases and actin dynamics (10, 12, 14, 56). It was recently shown in NIH 3T3 cells that stimulation of Rho- and actin dynamics-dependent signaling results in translocation of a novel SRF cofactor, myocardin-related transcription factor A (MRTF-A) (also called MAL or MKL1), from G-actin in the cytoplasm to the nucleus and in activation of SRF target genes (35).

In the present study, we investigated the role of MRTF-A in mediating prohypertrophic signaling evoked by mechanical stress and neurohumoral stimulation in cardiac myocytes. Our study defines Rho- and actin dynamics-dependent nuclear translocation of MRTF-A as a novel common mechanism transducing mechanical stretch and neurohumoral stimulation to activation of the hypertrophy gene program, including increased expression of the brain natriuretic peptide (BNP) gene, in cardiac myocytes.

MATERIALS AND METHODS

Plasmid construction. A DNA fragment from the 5′ flanking region of the human BNP gene (bp −423 to +98 relative to the transcription start site) was isolated by PCR using human genomic DNA as a template with the primers 5-ACT CGG AAG ATC TGT CTT GGC CGG GGC TGT TTT CGC-3 (sense) and 5-GAT TCC CAA GCT TCA TGT CTC TGG AGG GAC TGC GG-3 (antisense), after which the fragment was inserted upstream of a luciferase gene in the pGL3 vector using the BglII/HindIII sites (−423hBNP-luc). In addition, the following primers were used to generate deletion mutants in which the BNP 5′-flanking region from bp −146 to +98 (−146hBNP-luc), −77 to +93 (−77hBNP-luc), or −25 to +93 (−25hBNP-luc) were deleted: −146hBNP, 5-GGC GGA AGA TCT CGG AGG GGC TCA TTC CCG −3; −77hBNP, 5-GGC GGA AGA TCT TGC ATG GCA GGG CAG GCC-3; and −25hBNP, 5-GGC GGA AGA TCT CCC GAG GAG CCA GGA GGA-3. −1823hBNP-luc, human ANP promoter-reporter gene (−452hANP-luc), SM22α-luc, and 4× CArG-luc were described previously (21, 44). To generate a mutation in the CArG-like sequences of the BNP 5′-flanking region, PCR-based mutagenesis was performed using the primers 5-GGC CCA TTT CTG TAC CCG GTC GGC TCT G-3 (mut CArG sense) and 5-CAG AGC CGA CCG GGT ACA GAA ATG GGC C-3 (mut CArG antisense).

Cell culture and transfection. Primary neonatal rat ventricular myocytes were isolated and grown as described previously (37). Twenty-four hours after plating, the myocytes were transfected for 12 h with 200 ng of reporter plasmid and 200 ng of expression vector using the Gene Jammer reagent (Invitrogen) unless indicated otherwise. A Rous sarcoma virus (RSV)-driven *lacZ* expression vector was included in all transfections as an internal control. The transfectant cells were then incubated in serum-free medium for 6 h, after which ET-1 (100 nM), AngII (100 nM), or vehicle was added, and the cells were maintained for an additional 48 h.

Myocytes subjected to stretching were first transfected for 6 h with 300 ng of reporter plasmid using the Gene Jammer reagent (Invitrogen) unless indicated otherwise. The transfected cells were then incubated in serum-free medium for 12 h, after which they were subjected to 20% mechanical stretch for 4 h.

Recombinant adenovirus infection. For adenovirus production, cDNAs encoding FLAG-tagged, full-length mouse MRTF-A were cloned into the pAC-CMV vector, and the resultant constructs were cotransfected into HEK 293 cells along with pJM17 using Fugene 6 (Roche Applied Science). Clonal populations of adenoviruses were amplified by reinfecting HEK 293 cells, after which titers of the viral preparations were determined using the agar overlay method.

Thirty-six hours after plating, cardiac myocytes grown on coverslips in 6-well dishes were infected for 6 h with recombinant adenovirus at a multiplicity of infection (MOI) of 5 and then maintained in serum-containing medium for 24 h. Thereafter, the growth medium was replaced with serum-free medium, and cells were incubated for an additional 12 h before being treated with 100 nM ET-1 or AngII for 1 h and fixed in 4% formaldehyde in phosphate-buffered saline (PBS).

Thirty-six hours after plating on silicone membranes, cardiac myocytes were infected for 6 h with recombinant adenovirus at a MOI of 5 and then maintained in serum-containing medium for 36 h. After changing to serum-free medium, the cells were incubated for an additional 12 h and then subjected to 20% mechanical stretch for 1 h. The cells were then fixed in 4% formaldehyde in PBS.

The subcellular distribution of MRTF-A was determined by immunostaining for the FLAG epitope (green). Cardiac myocytes were also positively stained with anti-ANP antibody to distinguish them from cardiac fibroblasts (red).

Luciferase assay. Cells were harvested, and luciferase and control β-galactosidase activities were measured using a luciferase assay system (Promega) and a FluoReporter *lacZ* galactosidase quantitation kit (Invitrogen) according to the manufacturer's instructions. All assays were performed at least twice in triplicate.

EMSAs. Electrophoretic mobility shift assays (EMSAs) were performed using double-stranded oligonucleotides corresponding to the SM22 CArG or BNP CArG-like sequence. The probe sequences were as follows: SM22 CArG, 5′-CCT GCC CAT AAA AGG TTT TTC CTG CCC ATA AAA GGT TTT T-3′; BNP CArG, 5′-CAT TTC TAT ACA AGG TCG GCC ATT TCT ATA CAA GGT CGG C-3′; and BNP mutCArG, 5′-CAT TTC TGT ACC CGG TCG GCC ATT TCT GTA CCC GGT CGG C-3′. For gel mobility shift assays utilizing SRF, 2 μl of a coupled *in vitro* translation reaction product (TNT kit; Promega) was incubated with the indicated ^{32}P-labeled oligonucleotide probes in the presence of 1 μl of poly(dIdC) (1.5 μg/μl) for 20 min at room temperature, followed by nondenaturing electrophoresis. Unlabeled competitor oligonucleotides were added at a 10-, 100-, or 1,000-fold molar excess, and 2 μl of anti-SRF antibody (Santa-Cruz) was added for supershift experiments. The assay buffers and electrophoresis conditions were described previously (37).

ChIP assays. Chromatin immunoprecipitation (ChIP) assays were carried out according to the protocol supplied by the manufacturer (Upstate Biotechnology). Briefly, cultured ventricular myocytes fixed with 1% formaldehyde for 10 min at 37°C were collected, resuspended in SDS lysis buffer (1% SDS, 10 mM EDTA, and 50 mM Tris-HCl [pH 8.1]) containing 1 mM phenylmethylsulfonyl fluoride, 1 μg/ml aprotinin, and 1 μg/ml pepstatin A, and sonicated seven times for 10 s each time. After clearing the lysate by centrifugation, one aliquot of the lysate (20 μl) was removed to serve as an input control. The remainder was incubated overnight at 4°C in ChIP dilution buffer (16.7 mM Tris [pH 8.1], 167 mM NaCl, 1.2 mM EDTA, 1.1% Triton X-100, 0.01% SDS, 1 mM phenylmethylsulfonyl fluoride, 1 μg/ml aprotinin, and 1 μg/ml pepstatin A) also containing 20 μl of anti-SRF antibody (Santa Cruz). Thereafter, 60 μl of salmon sperm DNA and a protein G-agarose bead suspension were added and incubated for an additional 1 h at 4°C. The beads were then sequentially washed for 5 min each in low-salt immune complex wash buffer (20 mM Tris-HCl [pH 8.1], 150 mM NACl, 2 mM EDTA, 0.1% SDS, and 1% Triton X-100), high-salt buffer (20 mM Tris-HCl [pH 8.1], 500 mM NACl, 2 mM EDTA, 0.1% SDS, and 1% Triton X-100), LiCl immune complex wash buffer (250 mM LiCl, 1% Igepal-CA630, 1% deoxycholic acid [sodium salt], 1 mM EDTA, 10 mM Tris [pH 8.1]), and TE buffer (10 mM Tris [pH 8.0] and 1 mM EDTA). The immune complexes were then eluted by incubating the beads with elution buffer (1% SDS, 0.1 M $NaHCO_3$) for 15 min at room temperature. After the addition of 5 M NaCl, the eluates were heated to 65°C for 12 h to reverse the protein-DNA cross-links. The DNA was then recovered through proteinase K treatment, phenol-chloroform extraction, and ethanol precipitation. The resultant pellets were resuspended in 20 μl of TE buffer. PCR was performed with 2-μl samples of DNA using the following primers: rBNP CArG FW, 5-CAA TAC GGG TGG GGC ACG GTA-3; rBNP CArG RV, 5-ACC CCT CTG TGC CTC TGT-3; rBNP distal FW, 5-TGG CAC CAA GCC ACA CTC TGA AGA-3; rBNP distal RV, 5-GAA TGC TGC ATT TAA CGG CCT GGA T-3; rSM22 CArG FW, 5-GGT CCT GCC CAT AAA AGG TTT-3; rSM22 CArGRV, 5-TGC CCA TGG AAG TCT GCT TGG-3; GAP FW, 5-GCT CTC TGC TCC TCC CTG TT-3; GAP RV, 5-CAT CCT CTG CAA TGC GGA GC-3.

RNA interference. For analysis of MRTF-A using RNA interference (RNAi), a siGENOME Smart pool reagent against rat MRTF-A (M-081405-00-0010) with guaranteed minimum 75% mRNA knockdown was purchased from Dharmacon. A Block-It fluorescent oligomer (Invitrogen) was used as a nonspecific control. For luciferase assays, neonatal rat ventricular myocytes in Dulbecco's modified Eagle medium (DMEM) supplemented with 10% fetal bovine serum

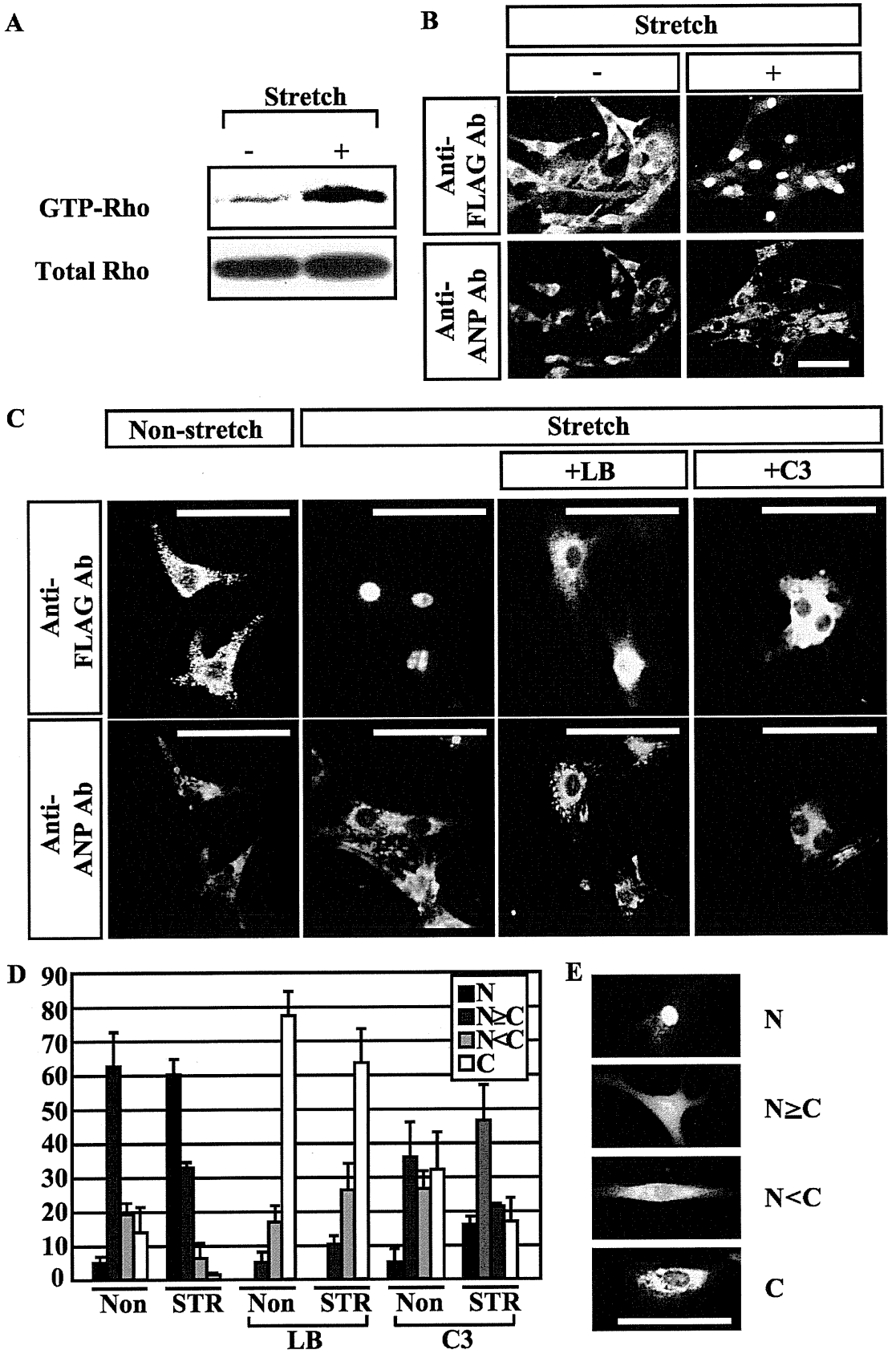
A
Stretch
- +
GTP-Rho
Total Rho
B
Stretch
- +
Anti-FLAG Ab
Anti-ANP Ab
C
Non-stretch
Stretch
+LB
+C3
Anti-FLAG Ab
Anti-ANP Ab
D
90
80
70
60
50
40
30
20
10
0
N
N≥C
N<C
C
Non STR Non STR Non STR
LB C3
E
N
N≥C
N<C
C

were transfected with 100 pmol of small interfering RNA (siRNA) and 500 ng of luciferase reporter plasmid for 12 h using Fugene. An RSV-*lacZ* expression plasmid was included in all transfections as an internal control. The transfectant cells were then incubated in serum-free medium for 6 h, after which ET-1 (100 nM) or vehicle was added, and the cells were maintained for an additional 48 h.

For luciferase assays with myocytes subjected to mechanical stretch, neonatal rat ventricular myocytes in DMEM supplemented with 10% fetal bovine serum were transfected with 200 pmol of siRNA and 600 ng of luciferase reporter plasmid for 12 h using Fugene. The transfected cells were then incubated for 12 h in serum-free medium, after which they were subjected to mechanical stretch for 4 h.

To verify the efficiency of siRNA-mediated knockdown of MRTF-A expression, rat smooth muscle cells in 6-well dishes were transfected with 200 pmol of siRNA and 48 h later were harvested for real-time reverse transcriptase PCR (RT-PCR) analysis. In cells transfected with rat MRTF-A siRNA, we observed an 88% reduction in the endogenous expression of MRTF-A mRNA compared to results for cells transfected with control siRNA.

To assess the effect of knocking down MRTF-A expression on myocyte hypertrophy, cells were transfected for 24 h using Lipofectamine with On-Target plus siRNA reagent for rat MRTF-A (Dharmacon) or control scrambled siRNA 2000, as previously described (46).

Animal experiments. MRTF-A$^{-/-}$ mice were kindly provided by E. N. Olson (University of Texas Southwestern Medical Center at Dallas) (26). The animal care and all experimental protocols were reviewed and approved by the Animal Research Committee at Kyoto University Graduate School of Medicine.

Thoracic aortic banding. Six- to 8-week-old male mice either underwent a sham operation or were subjected to pressure overload induced by thoracic aortic banding (TAB), as described previously (13). A constriction created using a 27-gauge needle was placed in the transverse aorta between the innominate and left carotid arteries. We previously showed that constriction to a 27-gauge stenosis induces moderate hypertrophy without clinical signs of heart failure or malignant ventricular arrhythmia. The mice were sacrificed 1 h (for acute pressure overload) or 3 weeks (for chronic pressure overload) after TAB. At that time, we confirmed the integrity of the banding by inspecting the surgical constriction and noting the marked difference in the caliber of the right and left carotid arteries.

Chronic AngII administration. AngII (dissolved in 10 mM acetic acid) was subcutaneously administered at the rate of 0.6 mg/kg of body weight/day for 2 weeks using an osmotic minipump (Alzet model 2002; Alza Corp.) implanted in each mouse at 10 weeks of age. After 1 week of AngII infusion, systolic blood pressure (SBP) was measured in conscious mice using a noninvasive computerized tail-cuff method (Muromachi).

Echocardiographic analysis. Cardiac function was evaluated echocardiographically in conscious 10-week-old mice using a Hewlett Packard Sonos 5500 ultrasound system with a 12-MHz transducer, as described previously (9). Briefly, views were taken in planes that approximated the parasternal short-axis view (chordal level) and the apical long-axis view. Left ventricular internal diameters and wall thicknesses were measured (at least 3 cardiac cycles) at the end of systole and the end of diastole.

Real-time RT-PCR. Total RNA was isolated from cultured neonatal ventricular myocytes or mouse hearts using Trizol and following the manufacturer's protocol. Real-time one-step RT-PCR was performed with 20 to 100 ng of total RNA using One-step RT-PCR master mix reagent (ABI). TaqMan primers and probes for mouse BNP, ANP, c-Fos, Egr-1, striated muscle activator of Rho signaling (STARS), skeletal α-actin, SM22α, and smooth muscle α-actin were purchased from ABI.

Statistical analysis. Data are presented as means ± standard errors of the means (SEM). Unpaired *t* tests were used for comparison between two groups, and analysis of variance (ANOVA) with *post hoc* Fisher's test was used for comparison among groups. *P* values of <0.05 were considered significant.

RESULTS

Nuclear translocation of MRTF-A in response to mechanical stretch in cardiac myocytes. Using a fibroblast cell line, MRTF-A was previously shown to be translocated into the nucleus following sequential serum stimulation and Rho activation and to then activate SRF (35). In cardiac myocytes, SRF is known to be involved in hypertrophic gene reprogramming (23, 32, 57), while Rho is known to be activated by various hypertrophic stimuli, including mechanical stretch and neurohumoral stimulation (with ET-1 or AngII) (1, 2, 5, 20, 24, 48, 52, 59). We therefore hypothesized that nuclear translocation of MRTF-A mediates the hypertrophic signaling evoked by mechanical stretch, resulting in activation of the hypertrophic gene program. To test that idea, we first examined whether MRTF-A is translocated into the nucleus in response to mechanical stretch in cultured neonatal ventricular myocytes infected with an adenovirus encoding MRTF-A. We initially confirmed that stretching cardiac myocytes in our system rapidly leads to Rho activation, as previously reported by others (1) (Fig. 1A). When we stretched cardiac myocytes expressing FLAG-tagged MRTF-A, we observed accumulation of MRTF-A in the nucleus within 1 h after the initiation of stretch (Fig. 1B, D, and E). This translocation of MRTF-A was blocked in the presence of latrunculin B, an inhibitor of actin treadmilling, or C3 exoenzyme, an inhibitor of Rho, which suggests Rho-actin dynamics plays a critical role in the stretch-induced nuclear translocation of MRTF-A (Fig. 1C and D).

Expression of BNP and other SRF-dependent fetal genes in response to acute pressure overload is impaired in MRTF-A$^{-/-}$ mice. We next tested whether loss of MRTF-A diminishes activation of the hypertrophic gene program induced by mechanical load *in vivo*. To evaluate the contribution of MRTF-A to mechanical stress-induced genetic alterations separately from the effects of subsequent neurohumoral activation, we subjected MRTF-A$^{-/-}$ mice to acute pressure overload. Under basal conditions, male MRTF-A$^{-/-}$ mice have no obvious structural or physiological deficiencies (26). Consistent with that finding, echocardiographic analysis revealed parameters of cardiac function to be similar in MRTF-A$^{+/+}$ (wild-type), MRTF-A$^{+/-}$, and MRTF-A$^{-/-}$ mice (unpublished ob-

FIG. 1. Mechanical stretch induces nuclear accumulation of MRTF-A in a Rho- and actin treadmilling-dependent manner. (A) Cardiomyocytes were subjected to 20% stretch for 5 min, after which GTP-RhoA was pulled down and visualized by Western blotting with anti-Rho antibody. (B) Cultured neonatal rat ventricular myocytes infected with adenovirus encoding FLAG-tagged MRTF-A (Ad-MRTF-A) were stretched by 20% for 1 h. The subcellular distribution of MRTF-A was determined by immunostaining for the FLAG epitope (green). Cardiac myocytes were positively stained with anti-ANP antibody (Ab) to distinguish them from cardiac fibroblasts (red). (C) Cultured neonatal rat ventricular myocytes infected with Ad-MRTF-A were stretched by 20% for 1 h in the presence or absence of an inhibitor of actin treadmilling (latrunculin B [LB]) or a Rho inhibitor (C3). The cells were then stained with anti-FLAG antibody (green) or anti-ANP antibody (red). (D) Graphs showing the percent MRTF-A localization in adenovirus-infected ventricular myocytes, with or without mechanical stretch, in the presence or absence of LB or C3. N, exclusive staining of MRTF-A in the nucleus; N≥C, nuclear staining of MRTF-A is greater than or equal to cytoplasmic staining; N<C, greater staining of MRTF-A in the cytoplasm than the nucleus; C, exclusive staining of MRTF-A in the cytoplasm. At least 100 infected cells were counted under each condition in three independent experiments. Values are means ± SEM. (E) Representative images of the four categories for MRTF-A localization are shown. In all images, bars represent 50 μm.

TABLE 1. Echocardiographic analysis of 11-week-old MRTF-A$^{+/+}$ and MRTF-A$^{-/-}$ mice treated with AngII or left untreated

Characteristic[a]	Value for mouse group[b]			
	No treatment		AngII treatment	
	WT	MRTF-A$^{-/-}$	WT	MRTF-A$^{-/-}$
HR (beats/min)	687.0 ± 40.0	694.8 ± 20.1	687.0 ± 20.9	677.4 ± 18.4
LVDd (mm)	2.92 ± 0.14	2.82 ± 0.33	2.7 ± 0.22	2.94 ± 0.09
LVDs (mm)	1.12 ± 0.15	1.04 ± 0.19	1.23 ± 0.09*	1.09 ± 0.12
IVST (mm)	0.95 ± 0.07	0.93 ± 0.01	1.03 ± 0.14	0.96 ± 0.06#
PWT (mm)	0.90 ± 0.06	0.90 ± 0.04	1.30 ± 0.17*	0.97 ± 0.05#
FS (%)	62.4 ± 4.3	63.6 ± 3.7	63.1 ± 2.3	66.0 ± 2.3
EF (%)	93.6 ± 1.9	94.6 ± 1.6	94.8 ± 1.1	95.6 ± 0.8
LVM (mg)	74.7 ± 4.8	80.5 ± 10.3	122.1 ± 11.5*	94.5 ± 4.7#

[a] HR, heart rate; LVDd, left ventricular end diastolic dimension; LVDs, left ventricular end systolic dimension; IVST, interventricular septal thickness; PWT, posterior wall thickness; FS, fractional shortening; EF, ejection fraction; LVM, left ventricular mass.

[b] Values are means ± SEM. For the untreated groups, $n = 5$; for the AngII-treated groups, $n = 8$ (wild type [WT]) or 9 (MRTF-A$^{-/-}$). *, $P < 0.05$ versus results for untreated (WT) mice. #, $P < 0.05$ versus results for WT mice treated with AngII.

servation; the data for wild-type and MRTF-A$^{-/-}$ mice are shown in Table 1). We evaluated the expression of three myocardin family genes and confirmed that ablation of MRTF-A expression produces no significant change in myocardin or MRTF-B mRNA levels (Fig. 2A). When we compared the heart weight-to-body weight (HW/BW) ratios and BWs of control MRTF-A$^{+/-}$ and MRTF-A$^{-/-}$ mice subjected to a sham operation or acute mechanical overload caused by TAB for 1 h (13), we found no differences among the four groups of mice (Fig. 2B and C). We then measured the levels of brain natriuretic peptide (BNP) and c-fos mRNA as representative markers of fetal cardiac genes and early response genes, respectively, 1 h after TAB in MRTF-A$^{-/-}$ mice and MRTF-A$^{+/-}$ mice (11, 28, 31). The c-fos gene contains a CArG box and an Ets-binding site and is regulated by the formation of a phosphorylated Elk-1/SRF complex independently of myocardin

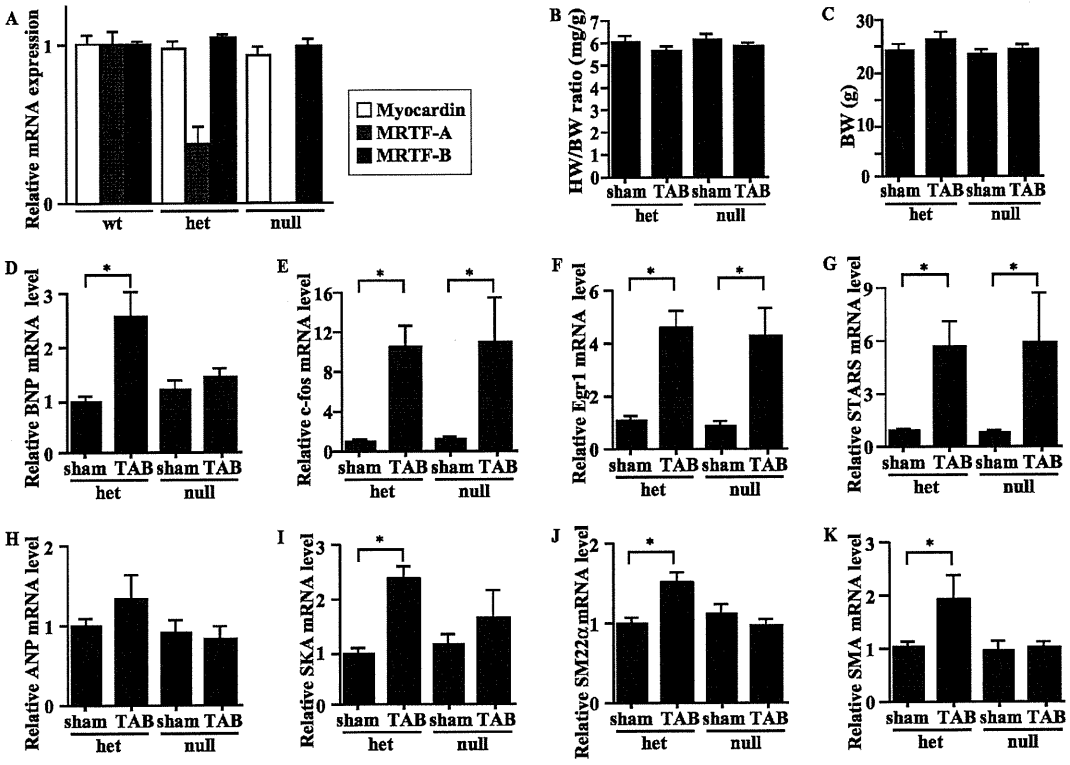

FIG. 2. The increased expression of BNP and SRF-dependent fetal cardiac genes induced by acute pressure overload is blunted in MRTF-A$^{-/-}$ mice. (A) Myocardin, MRTF-A, and MRTF-B mRNA levels evaluated by real-time RT-PCR in the ventricular myocardium of wild-type (wt), MRTF-A$^{+/-}$ (het), and MRTF-A$^{-/-}$ (null) mice. (B and C) HW/BW ratios (mg/g) (B) or BWs (g) (C) in 8- to 10-week-old MRTF-A$^{+/-}$ (het) and MRTF-A$^{-/-}$ (null) mice 1 h after TAB or sham operation ($n = 8$ each). (D to K) BNP (D), c-Fos (E), Egr-1 (F), STARS (G), ANP (H), skeletal α-actin (SKA) (I), SM22α (J), or smooth muscle α-actin (SMA) (K) gene expression was assessed by real-time RT-PCR using total RNA extracted from 8- to 10-week-old MRTF-A$^{+/-}$ (het) and MRTF-A$^{-/-}$ (null) mice 1 h after TAB or sham operation ($n = 8$ each). *, $P < 0.05$ versus results with sham. In all graphs, values are shown as means ± SEM.

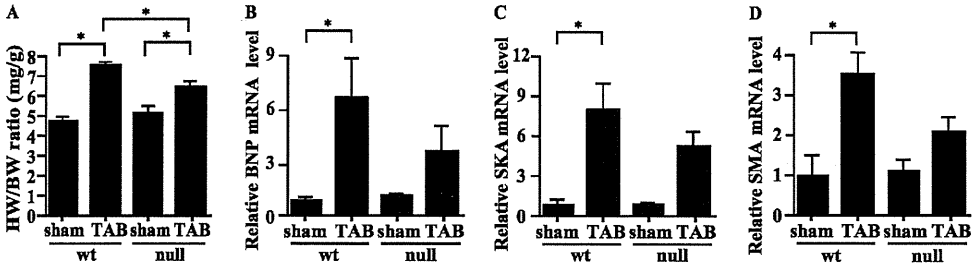

FIG. 3. Hypertrophic response induced by chronic pressure overload is attenuated in MRTF-A$^{-/-}$ mice. (A) HW/BW ratios (mg/g) in wild type (wt) and MRTF-A$^{-/-}$ (null) mice 3 weeks after TAB or sham operation ($n = 3$ each). *, $P < 0.05$. (B to D) BNP (B), skeletal α-actin (SKA) (C), or smooth muscle α-actin (SMA) (D) gene expression was assessed with real-time RT-PCR using total RNA extracted from wild type and MRTF-A$^{-/-}$ mice 3 weeks after TAB or sham operation ($n = 3$ each).

family coactivators (54, 61). As shown in Fig. 2D, the increase in BNP mRNA expression following TAB was markedly smaller in MRTF-A$^{-/-}$ mice than in their MRTF-A$^{+/-}$ littermates, though there was no significant difference in the induction of c-fos mRNA expression, which is indicative of the similarity of the mechanical stresses applied (Fig. 2E). Consistent with that finding, Egr-1, another early response gene known to be regulated by SRF independently of MRTF-A, was also similarly induced in the two genotypes (Fig. 2F) (54). In addition, the gene encoding the cytoskeletal protein striated muscle activator of Rho signaling (STARS), a downstream target of MEF2 also rapidly induced by TAB, was similarly activated in both genotypes (Fig. 2G) (21).

We also examined the expression of other known SRF target genes potentially controlled by myocardin family proteins, including the genes for ANP, skeletal α-actin, SM22α, and smooth muscle α-actin (53, 57). Though the level of ANP mRNA expression was not significantly altered by 1 h of TAB, levels of skeletal α-actin, SM22α, and smooth muscle α-actin gene expression were significantly upregulated in wild-type mice (Fig. 2H to K), but those increases were significantly attenuated in MRTF-A$^{-/-}$ mice (Fig. 2I to K). Thus, MRTF-A is required to mediate the stretch-induced hypertrophic signaling that leads to the upregulation of several SRF-dependent fetal cardiac genes.

To evaluate the contribution of MRTF-A to mechanical stress-induced chronic hypertrophic responses, including genetic alterations, we next subjected wild-type and MRTF-A$^{-/-}$ mice to chronic pressure overload. When we compared the HW/BW ratios in wild-type and MRTF-A$^{-/-}$ mice subjected to a sham operation or TAB for 3 weeks (13), we found that the increase in HW/BW ratios in MRTF-A$^{-/-}$ mice subjected to TAB was significantly smaller than those seen in wild-type mice subjected to TAB (Fig. 3A). Consistent with that finding, TAB-induced increases in the expression of genes encoding BNP, skeletal α-actin, and smooth muscle α-actin were significantly smaller in MRTF-A$^{-/-}$ mice than in wild-type mice (Fig. 3B to D). These results further support the notion that MRTF-A is required to mediate the mechanical stress-induced hypertrophic signaling that leads to upregulation of several SRF-dependent fetal cardiac genes.

BNP gene is a direct target of SRF. Although it has been suggested that BNP expression is under the control of SRF (43), a functional CArG box has yet to be identified in the BNP promoter, and it remains unclear whether BNP is a direct target of SRF. That said, the observed selective reduction of TAB-induced BNP expression in MRTF-A$^{-/-}$ mice suggests a direct involvement of SRF in BNP gene regulation. We previously showed that STARS induces nuclear translocation of MRTF-A and -B and activates SRF (19). To test whether BNP promoter activity is directly activated by SRF, we cotransfected COS1 cells with a BNP-luciferase gene and expression vectors encoding myocardin, MRTF-A, MRTF-B, or STARS. As shown in Fig. 4A, the BNP proximal promoter was activated by any of these SRF coactivators and was strongly activated by the combination of STARS and MRTF-A, clearly demonstrating that BNP is a MRTF-A-sensitive, direct downstream target of SRF. As in COS1 cells, the BNP promoter in cardiac myocytes was activated by myocardin, MRTF-A, and/or STARS and most strongly activated by the combination of STARS and MRTF-A (Fig. 4B).

We next used several BNP promoter deletion mutants to identify the response element for MRTF-A. We found that deletion from bp −423 to −146 significantly reduced the response of the BNP promoter to MRTF-A and STARS and that additional deletions did not reduce the activity further. This means the MRTF-A responsive element is located in a region between bp −423 and −146, within the BNP promoter (Fig. 4C). A search for a CArG box within this region revealed a sequence similar to a CArG box that extended from bp −184 to −193 (CTATACAAGG) and was completely conserved in humans, rats, and mice (Fig. 4D). We then performed electrophoretic mobility shift assays (EMSAs) using this sequence as a probe and found that SRF binds to the sequence but its affinity is weaker than that for the CArG box in the SM22α gene promoter (Fig. 5A). More importantly, we observed that endogenous SRF in cardiac myocytes binds to the sequence (Fig. 5A), and ChIP analysis confirmed the recruitment of SRF to this CArG-like sequence in the BNP gene in cardiac myocytes (Fig. 5B). Conversely, deletion or mutation of this element almost completely abolished activation of the BNP promoter by a SRF-VP16 fusion protein (Fig. 6A and B); moreover, mutations within this CArG element abolished the response of the BNP promoter to MRTF-A and STARS in both nonmuscle cells and cardiac myocytes (Fig. 6C to E), which makes this element the exclusive functional SRF binding site, at least within the 1,823-bp BNP promoter.

p300 is a transcriptional coactivator that possesses intrinsic histone acetyltransferase activity and reportedly participates in myocardin-mediated SRF activation (7). And because myocar-